T.R.
VAN YUZUNCU YIL UNIVERSITY
INSTITUTE OF NATURAL AND APPLIED SCIENCES
DEPARTMENT OF PHYSICS

# THE INVESTIGATION OF DOPING EFFECTS ON FORBIDDEN BAND GAP VALUE OF ZnO: EXPERIMENTAL AND THEORETICAL STUDIES

M.Sc. THESIS

PREPARED BY: Mahmood Hameed MAJEED
SUPERVISOR: Assoc. Prof. Dr. Murat AYCİBİN

VAN-2021

T.R.
VAN YUZUNCU YIL UNIVERSITY
INSTITUTE OF NATURAL AND APPLIED SCIENCES
DEPARTMENT OF PHYSICS

# THE INVESTIGATION OF DOPING EFFECTS ON FORBIDDEN BAND GAP VALUE OF ZnO: EXPERIMENTAL AND THEORETICAL STUDIES

M. Sc. THESIS

PREPARED BY: Mahmood Hameed MAJEED

VAN-2021

## ACCEPTANCE and APPROVAL PAGE

This thesis entitled "**THE INVESTIGATION OF DOPPING EFFECTS ON FORBIDDEN BAND GAP VALUE OF ZnO: EXPERIMENTAL AND THEORETICAL STUDIES**" and were prepared by Mahmood Hameed MAJEED under the consultation of Assist.Prof. Dr Murat AYCİBİN in Department of PHYSIC, on date of 15/ 1 /2021. It has been successful with a unanimous vote by the following jury and it has been recognized as a Master's Thesis according to Postgraduate Education and training regulation with the relevant provisions.

Supervisor: Prof. Dr. (NAME) Signature:

Member: Prof. Dr. (NAME) Signature:

Member: Assist. Prof. Dr. (NAME) Signature:

The Board of Directors of the Institute of Science: ...../...../..... date and is approved by decision No.....

Signature

.....

Director of the Institute

## THESIS STATEMENT

All information presented in the thesis were obtained in the frame of ethical behavior and academic rules. Also, all kinds of information that does not belong to me have been cited appropriately in the thesis prepared by the thesis writing rules.

Signature

Mahmood Hameed MAJEED

## ABSTRACT

**THE INVESTIGATION OF DOPING EFFECTS ON FORBIDDEN BAND GAP VALUE OF ZnO: EXPERIMENTAL AND THEORETICAL STUDIES**

MAJEED, Mahmood Hameed
M. Sc. Thesis, Department of Physics
Supervisor: Assoc. Prof. Dr Murat AYCİBİN
January 2021, 65 Pages

In this thesis**,** we used experimental and theoretical methods to investigate doping elements effects on the forbidden energy bandgap of ZnO compound. Mg, Y and Mg and Y together are used to produce a doped sample.

In the experimental part, the hydrothermal method was used to grow Mg, Y and Mg-Y co-doped ZnO compound. As seen from findings, while autoclave techniques have affected forbidden energy band gap of sample, the annealing temperature has not had any effects.

The absorbance data reveals that Mg, Y and Mg-Y co-doped ZnO have different absorbance behaviour. While ZnO doped with Mg, the absorbance data have shifted to the blue region, Y and Mg-Y coped ZnO absorbance have shifted to red region. Also, the transmittance data are suitable with absorbance data of sample.

In the theoretical part, the effects of doping elements are investigated after constructing supercell and replacing one or two Zn, depending on doping aim, with doping elements (Mg, Y, Mg-Y). Calculations shows that the forbidden energy band gap of the sample varies with type of dopant.



**Keywords**: Autoclave, Forbidden bandgap, Hydrothermal method, Optical properties, Wien2k.

# ÖZET

## ZnO'NUN YASAK BANT GAP DEĞERİ ÜZERİNDEKİ DOPİNG ETKİLERİNİN İNCELENMESİ: DENEYSEL VE KURAMSAL

MAJEED, Mahmood Hameed
Yüksek Lisans Tezi, Fizik Anabilim Dalı
Tez Danışmanı: Doç. Dr. Murat AYCİBİN
Ocak 2021, 65 Sayfa

Tez çalışmamızda, deneysel ve teoretik yöntemler kullanılarak zink oksit bileşiğinin yasak enerji bant aralığının katkı maddesi ile nasıl değiştiğini inceledik. Katkı elementleri olarak Mg, Y ve Mg-Y eş katkılı olarak kullanıldı.

Deneysel kısımda, Autoclave methodu, hidrotermal tekniği bir türü, kullanılarak katkılı örnekler elde edildi. Bu kısımda kullanılan autoclave metodondan sonra yapılan tavlamanın, hazırlanan örneklerin soğurma sonuçlarında bir etkisi olmadığı görüldü.

Soğurma grafikleri bize, katkı malzemesine bağlı olarak örneklerin soğurma grafiklerinin farklı olduğunu söylemektedir. ZnO bileşiği Mg ile katkılandığı zaman, soğurma mavi bölgeye kayarken, Y veya Mg-Y ile katkılandığı zaman soğurmanın kırmızı bölgeye kaydığı görülmüştür. Geçirme grafiği ise soğurma grafiğinin onaylayacak şekildedir.

Teorik kısımda, supercell oluşturulup, oluşturulan bu supercell de bir veya iki tabe Zn elementi, katkılanacak durumu göre, Mg, Y veya Mg-Y ile yerdeğiştirlmiştir. Bu şekilde elde edilen örneklerin yasak enerji bant yapılarındaki değişmeye bakılmıştır.

**Anahtar kelimeler:** Yasak bant aralığı, Wien2k, Hidrotermal yöntem, Otoklav, Optik özellikler.

adwq


## ACKNOWLEDGEMENT

In the name of Allah, the Most Gracious and the Most Merciful.

All praises to Allah and His blessing for the completion of this thesis. I thank God for all the opportunities, trials and strength that have been showered on me to finish writing the thesis.

First and foremost, I would like to sincerely thank my supervisor Assoc. Prof. Dr Murat AYCİBİN for his guidance, understanding, patience and most importantly, he has provided positive encouragement and a warm spirit to finish this thesis. It has been a great pleasure and honour to have him as my supervisor.

My deepest gratitude goes to all of my family members. It would not be possible to write this thesis without their support. I would like to thank my dearest father Hameed, my mother Bahar, my lover wife Avin, and my dear son Rawaz.

I would like to pay my special regards to Assoc. Prof. Dr Arife GENGER IMER for her patience and helping to understand the information behind experimental work. Also, I thanks to Dr Mahmood M. Kareem and Dr Ali.M.Mohammad for their help in the laboratory when I performed experiments. May God shower the above-cited personalities with success and honour in their life.

Also, I would like to thank to my jury committee members who is Prof. Dr Kenan SÖĞÜT, Assos. Prof. Dr. Gökhan UTLU, Assos. Prof. Dr. Arife G. İMER, Assos. Prof. Dr. Murat AYCİBİN and Asisst. Prof. Dr. Abdulkadir KORKUT, to listen and evaluate my work.

January, 2021

Mahmood Hameed MAJEED

## TABLE OF CONTENTS

**Page**

ABSTRACT.....i
ÖZET..... iii
ACKNOWLEDGEMENT.....v
TABLE OF CONTENTS ..... vii
LIST OF FIGURE ..... xi
LIST OF TABLES.....xiii
SYMBOLS AND ABBREVIATIONS .....xv
1. INTRODUCTION .....1
2. LITERATURE REVIEW.....3
3. THEORETICAL BACKGROUND .....5
3.1. Properties of Thin Film..... 5
3.2. Crystal Structure of Solid ..... 5
3.2.1. Wigner-seitz cell..... 7
3.2.2. Three-dimensional crystal lattice..... 7
3.3. Reciprocal Lattice ..... 8
3.4. Brillouin Zone..... 9
3.5. Semiconductor Material..... 10
3.5.1. Basic properties of semiconductor ..... 10
3.5.2. Density of electron and gaps ..... .11
3.6. Bandgap ($\boldsymbol{E_g}$)..... 12
3.6.1. Temperature dependence of the energy bandgap ..... 12
3.7. Electron transations.....13
3.7.1. Direct transation.....13
3.7.2. In direct transation.....14
3.8. ZnO Material Properties ..... 15
3.8.1. Crystal structure of ZnO ..... 15
3.9. Optical Constants..... 16
3.9.1. Extiniction coefficint ($k_o$) .....17
3.9.2. Dielectric constant.....17

**Page**

3.9.3. Absorption coefficient (α) ..... 18
3.10. Optical Properties of Crystalline Semiconductor..... 18
3.10.1. Transmittance (T) ..... 18
3.10.2. Reflectance (R)..... 19
3.10.3. Absorbance (A) ..... 19
3.11. Optical measure ment.....19
3.12. Annealing Process..... 20
3.13. Many-Particle Problem ..... 21
3.13.1. Born-oppenheimmer aproximation ..... 22
3.14. Density function theory ..... 22
3.15. WIEN2K Computational Program..... 24
4. EXPERIMENTAL PROCEDURE.....29
4.1. Hydrothermal System.....29
4.2. Materials and Method.....30
4.2.1. Substrates cleaning process ..... 30
4.2.2. Materials ..... 30
4.3. Preparation of (ZnO) Nanorod by Hydrothermal .....31
4.3.1. Preparation of ZnO seed layer ..... 31
4.3.2. Growth of ZnO nanorods..... 32
4.3.3. Role of zinc nitrate hexahydrate and hexamethylenetetramine (HTMA) 33
4.4. Co-dopping Process ..... 34
5. RESULTS AND DISCUSSION.....35
5.1. Optical Properties ..... 35
5.1.1. Absorbance ..... 35
5.1.2. Transmission..... 37
5.1.3. Optical energy bandgap ..... 38
5.2. Theoretical Study ..... 41
5.2.1. Volume optimizer ..... 41
5.2.2 Electron denisty..... .....44
5.2.3. Electronic properties of pure and doped ZnO.....44
6. CONCLUSION ……..……...47

**Page**

REFERENCES……49
EXTENDED TURKISH SUMMARY (GENİŞLETİLMİŞ TÜRKÇE ÖZET).....55
CURRCULUM VITAE .....65

## LIST OF FIGURE

**Figures** **Pages**

Figure 3.1. The classification of crystal-like (a) single crystal,(b) polycrystal, (c) amorphous. ..... 6

Figure 3.2. The space lattice of atoms, bases and bases crystal structure. ..... 6

Figure 3.3 Construction of the Wigner-Seitz cell. ..... 7

Figure 3.4 Three dimensional crystal structure and brave lattice. ..... 8

Figure 3.5 First and second Brillouin zone. ..... 10

Figure 3.6. Schematic temperature dependence of the electric conductivity for semiconductors. ..... 11

Figure 3.7 Position of Fermi level in different materials. ..... 12

Figure 3.8. shows the transition types (a) allowed direct transition, (b) forbidden direct transition, (c) allowed indirect transition (d) forbidden indirect transition . 15

Figure 3.9. Diagram showing parts of the UV-Vis spectrometer. ..... 20

Figure 3.10. The login screen of the WIEN2k computer calculation program. ..... 25

Figure 3.11. The screen on which the atomic positions of the WIEN2k computer..... 26

Figure 3.12. The atomic sphere in a unit cell. ..... 27

Figure 4.1. The image of Autoclave device..... 29

Figure 4.2. Sketch of preparing ZnO seed layers. ..... 31

Figure 4.3. Steps for preparing ZnO nanorods. ..... 32

Figure 4.4. Image of Teflon base to fix the glass substrates. ..... 34

Figure 4.5. Steps for preparing the ($Zn90Mg10 - xYxO$) films..... 34

Figure 5.1. The absorbance of the samples in the case (a) seed layer, (b and c) before and after annealing..... 36

Figure 5.1. The absorbance of the samples in the case (a) seed layer, (b and c) before and after annealing. (continues)..... 37

Figure 5.2. The transmittance of the samples for the case before and after annealed by 300°C. ..... 37

Figure 5.3. The energy bandgap for (a) seed layer, (b)ZnO, (c) $Zn90Mg10O$, (d) $Zn90Y10O$ , (e) $Zn90Mg5Y5O$. ..... 40

Figure 5.4. Energy (eV) vs. Volume $(a.u)$ plots of ZnO crystal under (a) LSDA, (b) WC-GGA, (c) PBE-GGA, (d) PBEsol-GGA, and (e) PBEsol+hf potentials. ..... 41

Figure 5.4. Energy (eV) vs. Volume $(a.u)$ plots of ZnO crystal under (a) LSDA, (b) WC-GGA, (c) PBE-GGA, (d) PBEsol-GGA, and (e) PBEsol+hf potentials.(continue) ..... 42

Figure 5.5. Pressure (GPa) vs. Volume (a.u) plots of ZnO crystal under (a) LSDA ,(b) 43

Figure 5.6. Three dimensional electron density for ZnO crystal. ..... 44

Figure 5.7. The band structure for ZnO, with PBEsol. ..... 44

Figure 5.8. The forbidden band structure for ZnO dopped by Mg. ..... 46

Figure 5.9. The band structure for PBEsol+hf. ..... 46

## LIST OF TABLE

**Table** **Page**

Table 3.1. Physical properties of ZnO.....16

Table 5.1. The experimental and lattice parameters of ZnO crystal obtained under PBE-GGA, LSDA, WC-GGA and PBEsol-GGA potentials.....42

## SYMBOLS AND ABBREVIATIONS

| Symbols | Description |
|---|---|
| $NRs$ | Nanorod structure |
| $ZnO$ | Zinc oxide |
| $Y$ | Yttrium |
| $Mg$ | Magnesium |
| $\sigma$ | Conductivity |
| $n$ | Mobil density of electron |
| $n(T)$ | Number of electron in the conduction band |
| $p(T)$ | Number of hole in the valence |
| $E_g$ | Forbidden bandgap |
| $k_g$ | Boltzmann constan |
| $T$ | Temperature |
| $E_c$ | Bottom of the conduction band |
| $E_v$ | Top of the valence band |
| $e$ | Electron charge |
| $I_0$ | Saturation current |
| $D_s$ | Density of states |
| $\varepsilon_s$ | The dielectric constant of semiconductors |
| $\varepsilon_i$ | The dielectric constant of an interfacial layer |
| $E_0$ | Ground state energy |
| $E_{xc}$ | Correlation energy |
| $E_f$ | Fermi energy |

| Abbrevations | Description |
|---|---|
| **EHF** | Hartree-Fock energy |
| **Ab-initio** | Basic principles method |

| Abbrevations | Description |
|---|---|
| **APW** | Replicated plane wave method |
| **DFT** | Density Functional Theory |
| **DOS** | Case Density |
| **GGA** | Generalized Gradient Approach |
| **LDA** | Local Density Approach |
| **LSDA** | Local Spin Density Approach |
| **LMTO** | Linear Muffin-tin Orbit method |
| **WİEN2k** | Computer Computing Program |

# 1. INTRODUCTION

In solid state physics, the thin-film technique is one of the important tools which has been used to develop semiconductor materials and give a clear idea on the properties of materials(Freund et al., 2004). With this technique, researchers can observe and measure semiconductors and metals, therefore, the findings can give a clear indication of their properties (Chopra, 2012). If layer or several layers of atoms of substance thickness is less than 1µm (1000 nm), this is called "Thin Films". The properties of thin films depend on bulk materials due to the dimensions of thin films. If we are dealing with 2D, the force will be applied on the particle which is located on the surface, on the contrary, the forces will apply from all direction in 3D ( Chopra, 1979).

Thin films are first made by (Busen & Grove) in 1852 by using Chemical Reaction. Also, Schafthaul used the hydrothermal techniques to the synthesis of tiny quartz crystals in Papain digester. In 1898, Barus worked on the saturation of glass with water to go below $200°C$ by using steel autoclaves. In 1959, Richard Feynman gave a talk, There's Plenty of Room at the Bottom, to explained hot to do the hiring, creating, and controlling materials on a micro-scale (Feynman,1960). Furthermore, the nanotechnology concepts have become common owing to the invention new instrument of nano-characterization tools, which assisted deeply study, modification and controlling of nanomaterials. subsequently, the film layer enhancement and its coated on certain plates have been chosen according to the desired study. The glass slides, silicon wafers, aluminum, quartz and others could be chosen to be used as a plate (Shan et al., 2004).

Due to their promising technological applications, the research in oxide metal/semiconductors have been developed step by step by using various methods for the growth of well-arranged metal oxide ($ZnO, SnO_2$ , $In_2O_3$)nanostructure. Pulsed laser deposition (PLD)(Okada et al., 2004), hydrothermal technique ( Liu et al., 1997), ion plating, chemical vapor deposition, spray pyrolysis technique (Bakr et al., 2015), and spin coating is the most widely used methods (Hou Wang et al., 2015).

The hydrothermal process can be regarded as the preferred approach due to the complexity and cost of most of the above-mentioned methods (Foo et al., 2014). To achieve the hydrothermal process, an autoclave is a tight steel cylinder that can withstand

a long period at high temperature and pressure (Kareem et al., 2020). The hydrothermal route is taken to grow some nanorods such as ZnO because of its cost-effectiveness, versatility and fast growth rate (Yim et al., 2012).

In this thesis hydrothermal technique was used to deposit metal on a slide glass substrate, owing to its special capabilities to form regular and pure thin films with various area dots for desirable purposes. ZnO NRs is hydrothermally synthesized on a glass substrate and annealed at various temperatures from 200 to 450°C. To obtain a high-quality nano-rod crystal and a low concentration of defect without a morphological change, the annealing temperature is required, with the same method, synthesized ZnO, ZnO: Mg and ZnO: Y. In brief, the seed layer has been used widely to grow NRs, which decreases the lattice mismatch between the NRs and the substrate as well as contributes to well-matched development NRs on a layer (Piticescu et al., 2006). Nanocrystalline forbidden bandgap, structure and morphology dependence on doping ratio has been studied. Also, the forbidden energy band gap of pure and Mg and Y doped ZnO were studied using Wien2K depending  Density Functional Theory.

The purpose of the thesis is to show doping effects on the forbidden bandgap of pure and doped ZnO hexagonal nanorods, this is important for technological areas which this compound could be a very good candidate for applications.

## 2. LITERATURE REVIEW

Mandal et al., in (2008) studied the structural and optical properties of zinc oxide membranes prepared using magnetron sputtering RF technique on glass bases with different temperatures 40, 100, 200, and 300$^{o}$C. The structural properties were studied and X-ray diffraction was shown. According to their findings, the optical properties showed that the transmittance of the membranes is high within the limits 90% of the visible area, and the value of the energy gap of the films ranged 3.24 - 3.3 eV.

Periasamy et al., in 2009 studied the annealing effect on the structural and optical properties of ZnO films. This sample was prepared by the vacuum coating technique on glass and silicon substrates. The forbidden energy bandgap of the sample increases from 3.05eV to 3.26 eV.

Ming Gao et al., in 2010 was studied ZnO nanoparticles with various yttrium-doping ratio were synthesized by sol-gel technology. The structural effects, morphologies and optical characteristics of the prepared samples were studied in depth by the effects of yttrium doping. The results showed that yttrium was successfully doped into ZnO matrix crystal lattice.

Shakti et al., in 2011 studied the effect of annealing on the optical and structural properties of zinc oxide membranes with different temperatures. The results of XRD sh owed that all the multi-crystalline membranes have a compact hexagonal crystal structure and that the particle size value for all membranes is less than 100 nm and suddenly increases when annealing at 400°C and decreases at 600°C. has a permeability of about 90% in the visible region and an optical energy gap of 3.21eV.

Han et al., in 2011 reported on the studied the energy bandgap and electronic properties on ZnO co-doped by magnesium and aluminium. He used not only an experimental method but also a theoretical method. According to their results, the bandgap and conductivity can be widely applicable to the doping level.

Zhang et al., in 2012 by used sol-gel method for synthesized yttrium doped ZnO according to this equation $Zn_{1-X}Y_XO$ with changing x values.

In 2013, the researcher Hainan Wu et al. was able to obtain ZnO nanoparticles deposited on the base (ITO) that were manufactured by the electrochemical method, and

they studied the effect of annealing temperature 300,400,and500°C on the surface morphology.

Kumar et al., in 2014 fabricated ZnOnanorod on seed layer (ITO)glass substrate was prepared by sol-gel and growth nanorod by hydrothermal method.

Sanjeev k.Sarma et al. in 2015 worked on yttrium doped ZnO nanopowder by hydrothermal precipitation method. Optical properties and microstructure of (YZO) were characterized.

Mohua Chakraborty et al., in 2015 using sol-gel and hydrothermal for studying structural and optical properties of ZnO was doped by copper on glass substrate .the grown thin-film nanorods samples were characterized using spectroscopy methods. Also, they used a computational method to evaluate and compare the optical properties of Cu-doped ZnO.

In 2016 researcher Tanumoy Debrath et al. was prepared yttrium doped ZnO nanoparticle by hydrothermal method at 400$^{o}$C. While they used XRD and FESEM to analyze the crystallinity and morphology of the sample, RAMAN was used to determine the different type of defect in the sample. Moreover, they showed that the optical properties of sample changes with increasing Y doping ratio in the compound.

In 2016, the researcher Guru Nisha Narayanan et al. Was able to obtain structures of ZnO nanoparticles using hydrothermal technology and by using a device.

Researcher Jong Won Choi et al, in 2019, made ZnO nanoparticles by using the hydrothermal method and studied the effect of annealing temperature 150 to 600°C on the surface morphology, crystal structures and defects of the rods.

M. Khuili et al., in 2020 reported on the studied the structure of the electron and optical properties of pure and Mg-doped ZnO nanosheets by used FP-LAPW method.

# 3. THEORETICAL BACKGROUND

In this chapter, we like to give some background information about the subject which is used in the thesis.

## 3.1. Properties of Thin Film

Thin film technology is one of the newest areas in condensed matter field. A thin film could be fabricated from any materials such as metals, semiconductors, metal oxides, metal nitrides, and/or mixed materials. In general, thin-film refers to a three-dimension range between 10 nanometers to 1000 nanometer. Thin-film adherence to the substrate is necessary because the film is inherently feeble. The substrate has a critical role in thin-film preparation for structural support. To get that support, the film must be attached to the substrate by strong forces. This makes for a robust film. Thin-film in research are greatly expanding around the world. During the last five decades, enormous research work has been devoted to any type of thin films. The most modern development in the field of thin-film physics is that of the optoelectronic devices.

To produce thin films, researches have been using different methods such as spray pyrolysis, spin coating, thermal evaporation and hydrothermal autoclave process.
Among the used methods, the hydrothermal autoclave process is one of the best methods to deposit thin film because of giving quality samples.

## 3.2. Crystal Structure of Solid

Crystal structures are formed by arranging atoms in three-dimensional space according to a certain geometric order. Crystals having a periodic order spread in all directions and show the same properties. The crystal structure allows us to have sufficient information about that substance by investigating a certain part of it. Crystals are classified into two class: single crystal (monocrystalline) and multi-crystalline (polycrystalline). If the structure of solid does not have a smooth shape and atomic order, this kind of structure are called amorphous structures.

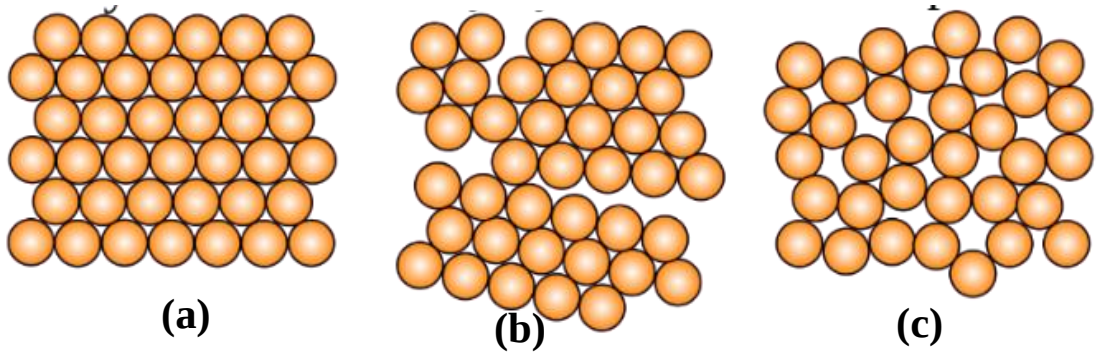


Figure 3.1. The classification of crystal-like (a) single crystal, (b) polycrystal, (c) amorphous.

The unit cell of the crystal contains all the symmetry properties of the crystal. The points where the atoms are located in the crystal are called lattice points, and the average distance between two atoms is called the lattice constant.

If the crystalline unit cell contains an atom, it is called a simple lattice. If it contains two or more atoms, it is called a composite lattice. If there is more than one atom in the unit cell, the positions of the atoms relative to the centre of the cell are called "bases". The translation vector joining two consecutive mesh points in the crystal is called the base vector. Can be formulated the crystal structure briefly:

Crystal =lattice + basis

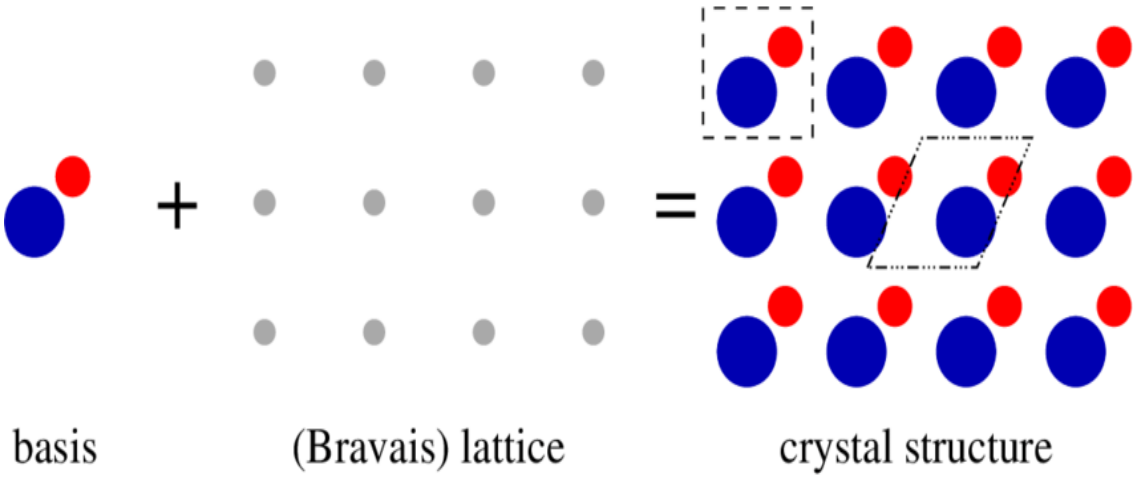


Figure 3.2. The space lattice of atoms, bases and bases crystal structure.

### 3.2.1. Wigner-seitz cell

The Wigner-Seitz cell is the cell of the crystal structure that occupies the smallest volume/area and has all the properties of the crystal (Kittel, 2014). With this cell, space can be filled absolutely as shown in the figure (3.3).

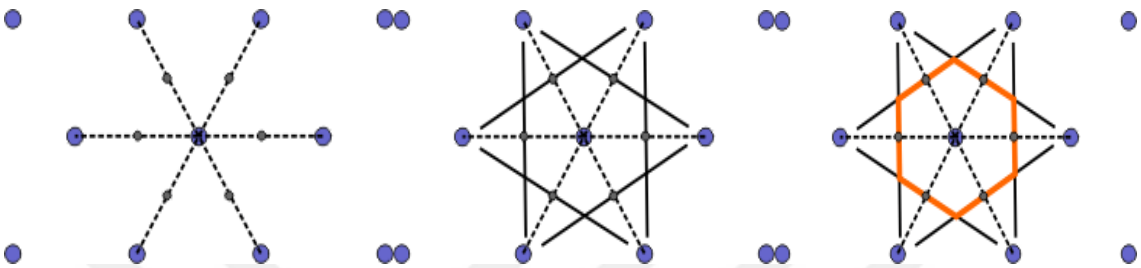

Figure 3.3 Construction of the Wigner-Seitz cell.

### 3.2.2. Three-dimensional crystal lattice

A three-dimensional crystal lattice; It is defined using three basic lattice constants such as $a_1, a_2, a_3$. These are also primitive vectors of the crystalline lattice. The equilibrium states of the lattices forming the crystals create a three-dimensional symmetrical shape. Due to this uniform distribution, the appearance of the crystal is the same everywhere. If we translate any point $\vec{r}$ on the crystal to a new point $\overrightarrow{r'}$, the relationship between these two points are shown as follow:

$$\overrightarrow{r'} = \vec{r} + n_1 a_1 + n_2 a_2 + n_3 a_3 \tag{1}$$

where $n_1, n_2$ $and$ $n_3$ are any integers.

In addition to translation, rotation, reflection and inversion symmetry processing can also be applied in crystals (Othman, 2009). Due to the restrictions created by symmetry operations, the lattice systems that are 5 in two dimensions and 7 in three dimensions. These structures may show different variations within themselves. Thus, 14 lattice systems in three dimensions are possible. It is called the Bravais lattice system. In a Bravais lattice, all lattice points are equivalent. The existence of equivalent structures indicates that all atoms in the crystal are of the same kind. If the mesh has non-Bravais

structure, some of the lattice points are equivalent and some are not. A mesh is created in space with the entire set of translation. Any translation in space is defined by a crystal translation vector denoted by $T$, as the complete multiples of primitive vectors $a_1, a_2\ vs\ a_3$ and also, any point on the lattice can be translated into each other with the help of translation vectors (Othman, 2009).

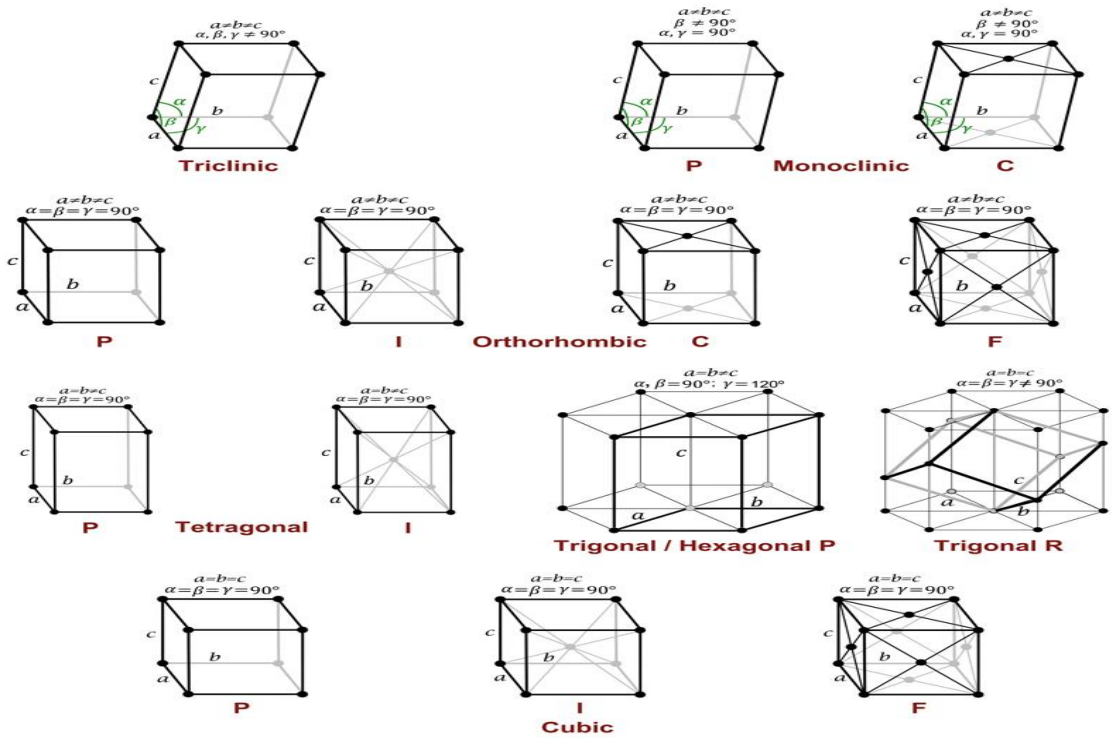


Figure 3.4 Three-dimensional crystal structure and brave lattice.

### 3.3. Reciprocal Lattice

Reciprocal lattices have an important place in an analytical examination of crystal systems. Most of the crystal structure, electrical and optical properties of semiconductor materials and metals can be explained with the help of reciprocal lattice. The axis vectors of the reciprocal lattices are defined by $\vec{b}_1, \vec{b}_2 and\ \vec{b}_3$ , they are also primitive vectors of the inverse lattice (Turgut, 2014). The unit of reciprocal vectors is the inverse of the unit of vectors in real space ($m^{-1}$). There are a crystal lattice and a reciprocal structure (k - space) for each crystalline structure. There is a relationship between reciprocal vectors and real lattice vectors shown in equations 3,4 and 5. (Kittel, 2014).

$$\vec{b}_1 = 4\pi \frac{\vec{a}_2 \times \vec{a}_3}{\vec{a}_1.(\vec{a}_2 \times \vec{a}_3)} \tag{2}$$

$$\vec{b}_2 = 4\pi \frac{\vec{a}_3 \times \vec{a}_1}{\vec{a}_1.(\vec{a}_2 \times \vec{a}_3)} \tag{3}$$

$$\vec{b}_3 = 4\pi \frac{\vec{a}_1 \times \vec{a}_2}{\vec{a}_1.(\vec{a}_2 \times \vec{a}_3)} \tag{4}$$

Each vector defined in Equations 3, 4 and 5 is perpendicular to the other two axis vector of the crystal lattice. Hence the reciprocal vectors:

$$\vec{b}_i \,.\, \vec{a}_j = 2\pi\delta_{ij} \tag{5}$$

The general translation vector for reciprocal points is $\vec{G} = v_1\vec{b}_1 + v_2\vec{b}_2 + v_3\vec{b}_3$ , Then $v_1$ , $v_2$ , $v_3$ used here are integers.

### 3.4. Brillouin Zone

The Wigner-Seitz cell in real space is defined as the first Brillouin region (BZ) in k-space. The first BZ cell is determined as follows a vector $\vec{b}$ is drawn from its origin to the nearest reciprocal point and the smallest volume formed by planes intersecting this vector in the middle is defined as the first BZ. Also, Brillouin regions have an important place in the calculation of the crystalline electronic energy band. The Brillouin structure has all k vectors that will give the reflections of Bragg's law from crystal (Kittel, 2014).

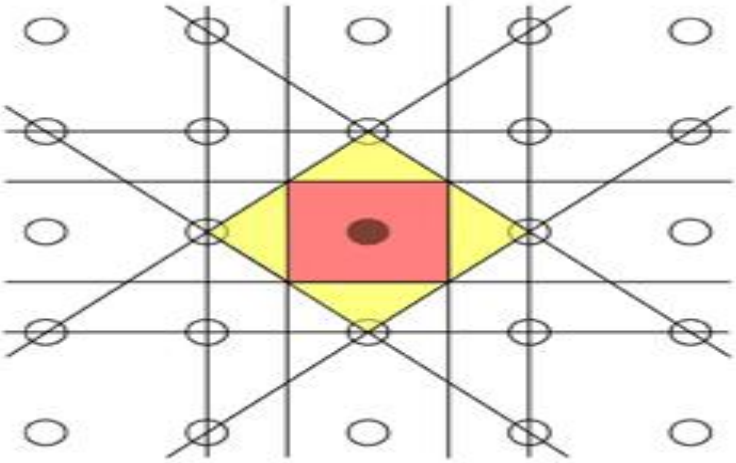

Figure 3.5 First and second Brillouin zone.

### 3.5. Semiconductor Material

If the material has electrical resistivity lying in the range of $10^{-2} - 10^{9}\Omega$.cm, a semiconductor it is classified as a semiconductor according to many solid-state textbooks. Also, the band gap has been used to define a material. The energy gap of semiconductors for electronic excitations lies bigger than 0 and smaller than 4 electron volts (eV)(Pillai, 2008).

#### 3.5.1. Basic properties of semiconductor

semiconductors are between metals and insulators according to electrical conductivity. For semiconductors, the conductivity decreases upon cooling as shown in figure (3.6) and the conductivity are given following:

$$\sigma = \frac{\mathrm{ne^2t}}{\mathrm{m}} = \mathrm{Cexp}\left(\frac{-\mathrm{E_g}}{\mathrm{2KT}}\right) \tag{6}$$

where $n$ is the density of mobile electrons, t is the average time between two scattering events of the electrons, m is mass of charge and e is the electronic charge, respectively.

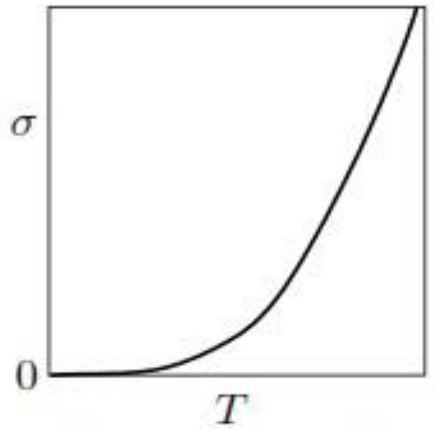


semiconductor/insulator

Figure 3.6. Schematic temperature dependence of the electric conductivity for semiconductors.

On the contrary, there are no mobile charges in insulators and semiconductors at $T = 0°C$. At finite temperature, charges are excited by thermal energy to overcome the bandgap $E_g$ between the valence and the conduction band.

$$n = n_o \left(\frac{T}{T_o}\right)^{\frac{3}{2}} \exp\left(\frac{-E_g}{2K_B T}\right) \tag{7}$$

where $T_0 = 300K$ and $n_o$ is electron density and it is typically $10^{20} cm^{-3}$. Consequently, the charge carrier density at room temperature is around $n \sim 10^{-27} cm^{-3}$. For a higher charge carrier density means the smaller energy band gaps. Materials with a smaller bandgap in this command are not fully isolating, therefore, termed semiconductors.

### 3.5.2. Density of electron and gaps

In quantum mechanics, the Fermi energy is the highest energy level which is occupied level in a system of fermions at absolute zero temperature(Ferreira et al., 2008). Fermi-Dirac distribution function indicates the probability of the position of an electron.

$$f = \frac{1}{1 + e^{\left(\frac{E - E_F}{k_B T}\right)}} \tag{8}$$

where $E_F$ is the Fermi Energy, $k_B$ is the Boltzmann constant and T is the temperature(Kittel et al., 1996). Fermi level shows different materials in the following figure (3.7).

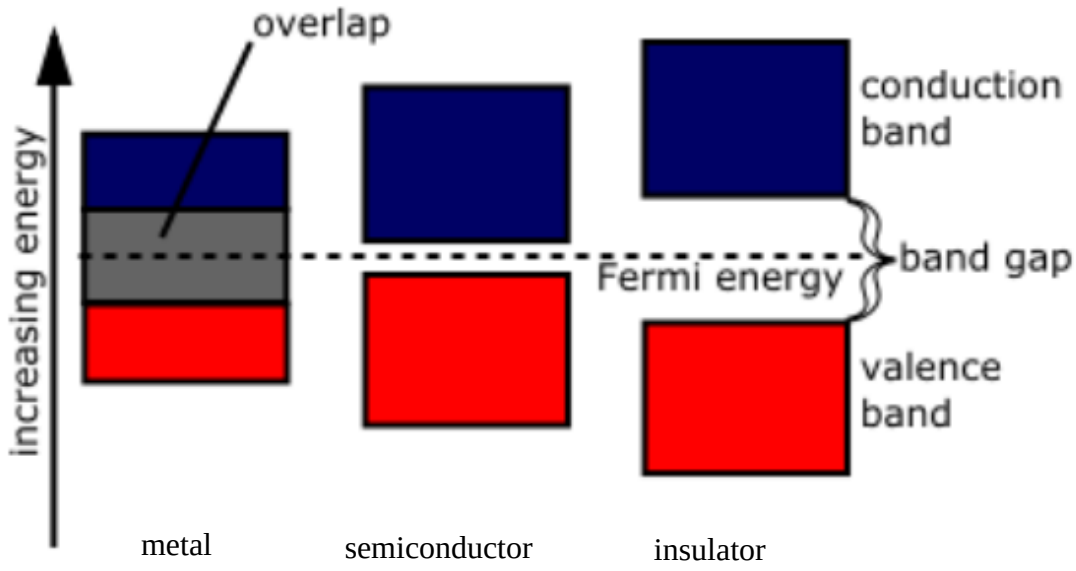


Figure 3.7 Position of Fermi level in different materials.

### 3.6. Bandgap ($E_g$)

The bandgap is the energy gap between the highest point of the valance band and the lowest point of the conduction band in the energy band graph. Depending on the increased temperature value, electrons are thermally excited and they might be transited from the valance band to the conduction band. The bandgap to temperature ratio controls the intrinsic conductivity and intrinsic carrier concentrations. When this ratio is large, both of the concentration of intrinsic carriers and conductivity will below.

#### 3.6.1. Temperature dependence of the energy bandgap

The energy bandgap of the semiconductors begins to reduce accordingly the temperature goes up. Also, the interatomic space can be more clear if the amplitude of the atomic vibrations changes because of raised thermal energy. The linear expansion

coefficient of a substance quantifies this effect. The effective potential observed by electrons in the substance is decreased by an increased interatomic spacing, which is the size of energy bandgap become reduced(Zhang et al., 2008). Direct interatomic distance modulation, such as the application of compressive stress (tensile) leads to an increase or decreases of the bandgap. The energy bandgap temperature dependency, $E_g$, has been experimentally determined to provide the following term for $E_g$ as the temperature function, And the energy could be well represented using the equation of Varshni (Varshni, 1967).

$$E_g(T) = E_g(0) - \frac{\alpha T^2}{T + \beta} \tag{9}$$

Where $E_g(0)$, αand $\beta$ are the fitting parameters. These fitting parameters are listed for germanium, silicon, and gallium arsenide.

### 3.7. Electron Transitions

The electronic transitions could be enamurated according to electron passing path valance band to conduction band:

#### 3.7.1. Direct transition

Direct transition takes place when one electron transits from valance band to conduction band which are located at the same high symmetry point. It can be divided into two types:

a) Direct allowed transition

From figure (3.8a) shows that the transition occurs when the top points in the (V.B.) matches exactly to the bottom point in the (C.B.).The general relationship for this type of transition is given.

$$\alpha h\nu \approx \left(h\nu - E_g\right)^{1/2} \tag{10}$$

where $E_g$ is an energy gap between direct transition, $\alpha$ is absorption coefficient and υ is the frequency of the incident photon.

b) Direct forbidden transition

If top point of valance band located close to bottom of the conduction band, this type of tranmisson is named as the direct forbidden transition as shown in figure (3.8.b), The equation for this transitions type given by:

$$\alpha h\nu \approx \left(h\nu - E_g\right)^{3/2} \tag{11}$$

**3.7.2. Indirect transition**

In these transitions type, the bottom of (C.B.) is not located at the high symmetry point like the top of (V.B.), in the curve (E-K). When the electron transits from (V.B.) to (C.B.), it needs extra momentum and this transition type takes place with help of the particle is called "Phonon", for the conservation of the energy and momentum law. There are two types of indirect transitions, they are:

a) Allowed indirect transition

Figure (3.8c) shows an allowed indirect transition and the formulea is given following.

$$\alpha h\nu \approx \left(h\nu - E_g\right)^{2} \tag{12}$$

b) Forbidden indirect transition

If the transition occurs from any point of valance band other than the bottom of the conduction band which is located at the same high symmetry point, This is called the forbidden indirect transition ands it is screcthed in figure(3.8).

$$\alpha h\upsilon \approx \left(h\nu - E_g\right)^3 \qquad (13)$$

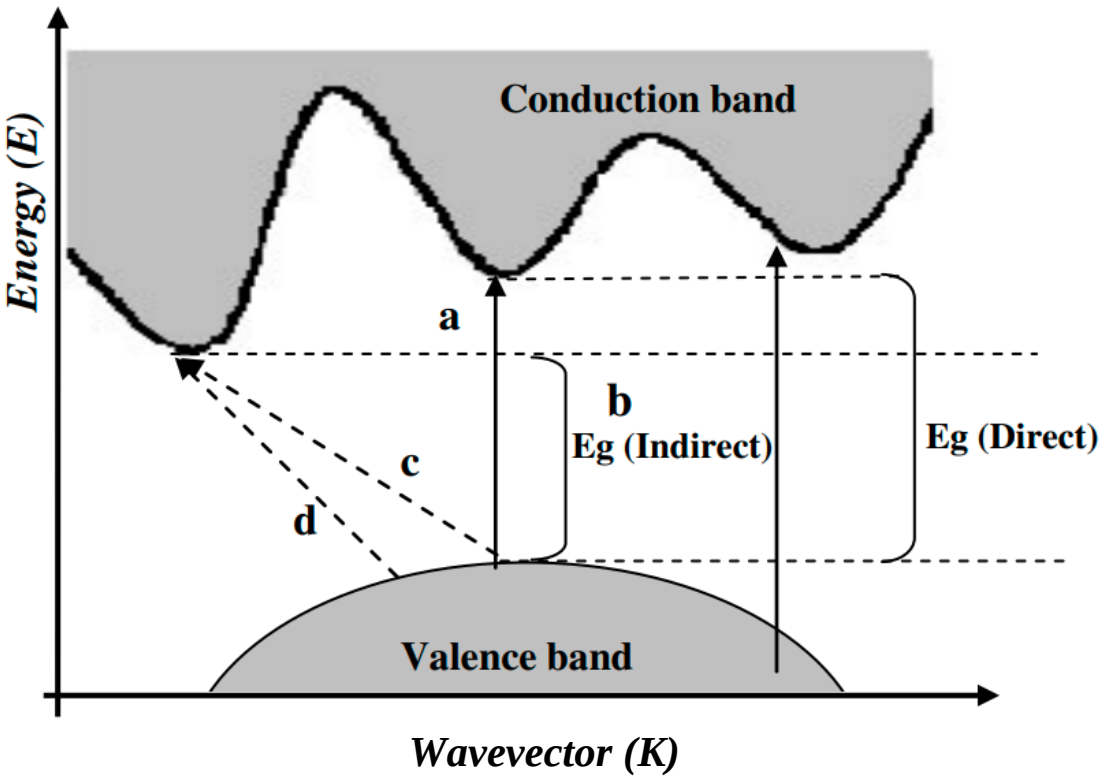


Figure 3.8. The transition types (a) allowed direct transition, (b) forbidden direct transition, (c) allowed indirect transition (d) forbidden indirect transition

### 3.8. ZnO Material Properties

In the materials science, Zinc Oxide is classified as a semiconducting compound with a wide bandgap in the near-UV spectral region. ZnO crystallizes in the wurtzite structure. İt has very unique properties at room temperature which makes it a very

desirable compound in the electronic, optoelectronics and laser technologies for researchers (Bacaksiz et al., 2008-Wang et al. 2005).

Pyro- and piezo properties of ZnO makes compound being used in sensor, converter, energy and generator areas(Wang, 2008, Chari et al., 2012). In table 1, you can see the physical properties of compounds.

Table 1. Physical properties of ZnO

| Properties | Value |
|---|---|
| Band gap (eV) | 3.1-3.37 |
| Coefficient of thermal expansion x$10^{-6}$/°C | $\alpha_{11}$=4.0<br>$\alpha_{33}$=2.1 |
| Thermal conductivity | 100 mW/cm.K at 300K |
| Colour | White |
| Crystal structure | Wurtzite |
| Density(g/$cm^3$) | 5.61 |
| Lattice constant (°$A$) | 3.253 |
| Melting point (°C) | 1975 |
| Optical transparency (μm) | 0.4-2.5 |
| Refractive index | 2.008 |
| Electron effective mass | $0.24m_o$ |
| Electron Hall mobility at 330K | $200\ {cm^2}/{Vs}$ |
| Hole effective mass | $0.59m_o$ |
| Sublimation temperature (°C) | 1975 |
| Exciton binding energy | 60meV |
| Type of conductivity | n-type |

### 3.9. Optical Constants

Refractive index (n), extinction coefficient (k) is the important parameters for the optical properties of the material. Refractive index is given the following.

$$n = \left[\left(\frac{4R}{(R-1)^2}\right) - {k_o}^2\right]^{1/2} - \frac{R+1}{R-1} \tag{14}$$

where n is the refractive index, R is the reflectance

### 3.9.1. Extinction coefficient ($k_o$)

The extinction coefficient ($k_o$) give information about loss of energy when electron propagates through the material and it is given.

$$k_o = \frac{\alpha\lambda}{4\pi} \tag{15}$$

where λ is the wavelength of the incident radiation and α is given by

$$\alpha = \frac{2.303A}{t} \tag{16}$$

A stands for absorbance, and t is used to describe sample thickness. So, the reflection is calculated from the following equation.

$$R + T + A = 1 \tag{17}$$

### 3.9.2. Dielectric constant

A complex dielectric constant characterizes an absorbing medium.

$$\varepsilon = \varepsilon_1 + i\varepsilon_2 \tag{18}$$

So that

$$\varepsilon_1 = n^2 - {k_o}^2 \tag{19}$$

$$\varepsilon_2 = 2nk_o \tag{20}$$

where $\varepsilon_1$ and $\varepsilon_2$ are real and imaginary part of dielectric constant.

### 3.9.3. Absorption coefficient (α)

When photon energy incidents are much less than the energy gap, so the photon transmits and the thin- film is transmitted by the relationship (Ilican et al., 2008):

$$T = (1 - R)^2 e^{-\alpha x} \tag{21}$$

and the absorption coefficient can be estimated from the absorbance using the formula.

$$\alpha = \frac{(2.303 * A)}{t} \tag{22}$$

## 3.10. Optical Properties of Crystalline Semiconductor

Researchers spend their time to reveals the optical properties of a material for many reasons. Firstly, In the interference filters, optical fibres and reflective coating technologies require accurate knowledge of optical constants of medium over a wide range of wavelengths. Secondly, the optical properties of all materials could give information about their atomic structure, electronic band structure, and electrical properties.

### 3.10.1. Transmittance (T)

Transmittance (T) is given by the ratio of the intensity of the rays ($I_T$) transmitting through the film to the intensity of the incident rays ($I_O$) as follows ( Fox, 2001):

$$T = \frac{I_T}{I_O} \tag{23}$$

$$T = \frac{(1 - R)^2 e^{-\alpha x}}{1 - R^2 e^{-2\alpha x}} \tag{24}$$

### 3.10.2. Reflectance (R)

*R* is related to the refractive index and extinction coefficient of the material as follows (Pankove, 2012):

$$R = \frac{(n-1)^2 + {k_o}^2}{(n+1)^2 + {k_o}^2} \tag{25}$$

where n: Refractive Index, $k_o$ **:** Extinction Coefficient.

### 3.10.3. Absorbance (A)

Absorbance can be defined as the ratio between absorbed light intensity ($I_A$) by material and the incident intensity of light ($I_O$) (Mark Fox, 2002):

$$A = \frac{I_A}{I_O} \tag{26}$$

## 3.11. Optical Measurement

Optical measurements of the absorbance, A, and transmittance, T, of the wavelength range(200-1100nm) for all prepared films was performed using the UV-spectroscopy (Shimadzu) Japanese-made type (UV - Visible2600 Spectrophotometer). The experimental step was sketched in figure(3.9). As you can see from the figure that, a very clean glass slide placed inside the reference section and sample was placed inside the sample section. After, the beam is projected vertically once on the glass s and sample simultaneously. Finally, the transmittance rate was measured and all the results for the prepared film from the absorption and permeability spectrum with the absorption coefficient, and the energy band gap will be calculated.

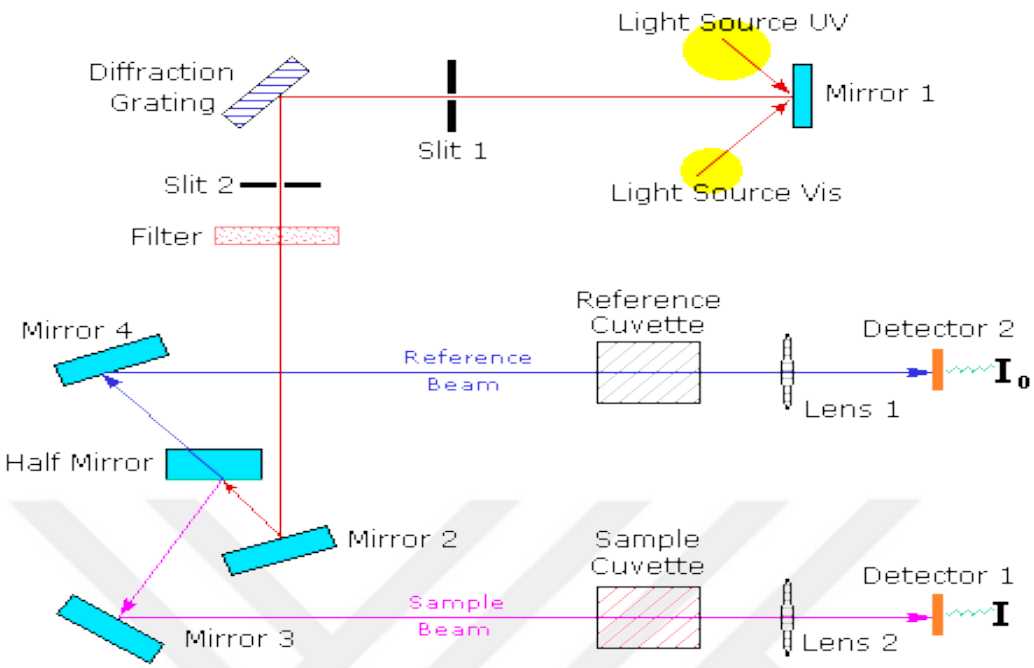


Figure 3.9. Diagram showing parts of the UV-Vis spectrometer.

### 3.12. Annealing Process

The annealing process is characterized as the process of exposing a thin model or membrane to a specified temperature for a limited period. Generally carried out in a vacuum and the presence of air or the presence of a specified gas. And, this is done according to the below rules.

1. Reducing the structural defects provide kinetic energy to the atoms. And with this extra energy, the atoms can be reorganized into the crystal structure. Moreover, the structural properties can be affected by temperature, time and environment annealing conditions etc.
2. It results in the interaction of the membrane material with oxygen while the annealing is performed in an air space. It is thus considered an effective process for the preparation of a certain oxide, such as $SnO$ and ZnO.
3. Conversion of the corresponding membrane composed of several materials or one substance from random to polycrystalline or multi-crystalline to monocrystalline.

4. Elimination of most defects, such as stack faults and eruptions and stress reduction generated(Muchuweni et al., 2018).

However, those would have a tremendous difficulty to achieve good crystal quality as the higher temperature does not increase the simple defects and so the moaning temperature must be changed to obtain a high and pure crystal., (Choi et al., 2019). The rationing is divided into two types:

1. Rapid thermal annealing.
2. The classical thermal annealing: the process can be done in three steps.
   - Heated to the required temperature.
   - Balancing the desired temperature for a while.
   - Cooled to room temperature.

### 3.13. Many-Particle Problem

Molecules made up of atoms and solids consisting of them cause a large number of particles to come together and interact with each other. It is not possible to describe the energies of such multi-particle and continuously interacting systems in real-time. It becomes necessary to benefit from quantum equations in the solution of these systems consisting of atoms and molecules (Akkuş, 2007). Every problem with the electronic structure of matter involves the time-dependent Schrödinger equation. However, in many cases, we can be satisfied with the timeless Schrödinger equation. For an atomic or molecular system of N electrons, the equation shows that.

$$\widehat{H}\Psi = E\Psi \tag{27}$$

where E is the electronic energy value, $\widehat{H}$ Hamiltonian operator and $\Psi = \Psi$ (1, $x$ 2,… $x$ $n$) wavefunction. The hamiltonian processor of the multi-particle system is written as expanded.

$$\widehat{H} = \widehat{T}_e + \widehat{T}_i + \widehat{V}_{ii} + \widehat{V}_{ie} + \widehat{V}_{ee} \tag{28}$$

wherein this equation $\hat{T}_e$ the kinetic energy of electrons, $\hat{T}_i$ the kinetic energy of the ion, $\hat{V}_{ie}$ ion-ion interaction potential energy, $\hat{V}_{ie}$ is ion-electron interaction potential energy and $\hat{V}_{ee}$; is the electron-electron interaction potential energy. If the Hamiltonian processor of a perfect crystal is written explicitly (Yu, 2001).

It is not possible to solve this equation in real-time. can be required by some approximation like Hartee.

### 3.13.1. Born-oppenheimmer approximation

In the Born-Oppenheimer approximation, the nucleus (core) is almost stationary compared to the electron. When we consider this approximation, the kinetic energy $\hat{T}_i$ of the core ion given in equation, 28 is neglected.

The ion-ion interaction potential energy $\hat{V}_{ii}$ can be added to the system as a constant number. In this case, the equation can be written as equation 29.

$$\hat{H} = \hat{T}_e + \hat{V}_{ie} + \hat{V}_{ee} = \sum_i \frac{{P_i}^2}{2m_i} - \sum_{j\prime i} \frac{Z_j e^2}{|r_i - R_j|} + \frac{1}{2}\sum_{i,i\prime} \frac{e^2}{|r_i - r_{i\prime}|} \tag{29}$$

Thus, the Hamiltonian expression in equation 28 can be written as in equation 29. (Yu, 2001).

In this equation, all terms are related to the electron. However, the solution in the Born-Oppenheimer approximation equation 28 is still complex due to a large number of electron-electron interactions. This approach is also invalid when the electron and nucleus do not move together and separate from each other. The equation has been simplified by contributions made by Hartree.

## 3.14. Density Function Theory

Density Functional Theory (DFT) is a method which depends on the electron density of the molecule. Unlike the wave function, the electron density is a physical

characteristic of all molecules. The main idea of DFT is to use the simple electron density $\rho(r)$ instead of N-electron wave function.

Hohenberg and Kohn (H-K) were the first to offer an approximation. The electron density is a function of x,y and z space coordinates. The first H-K theorem states that the ground state energy of an N-electron system in an external potential V(r) is a unique functionality of its ground state electron density ρ(r):

$$\rho_{(r_1)} = N \int \left|\Psi\left(\vec{x}_1, \vec{x}_2, \dots \vec{x}_N;\ \vec{R}_1, \dots, \vec{R}_{Nn}\right)\right|^2 d\sigma_1 d\vec{x}_2\, d\vec{x}_N \tag{30}$$

The integral of the density over all space equals N. The total energy can be written as:

$$E[\rho] = T[\rho] + V_{ee}[\rho] + \int \rho(\vec{r})\ V(\vec{r})\, d\vec{r} \tag{31}$$

Later, Kohn and Sham (KS) invented an indirect way of calculating the kinetic energy functional thereby making the DFT method as an efficient tool for carrying out rigorous calculations.

The KS method relies on the introduction of fictitious reference systems of non-interacting electrons that are constructed to have the same electron density as the system of interest. In this method, kinetic energy could be expressed for the reference system as the sum of the expectation value of the Laplacian for each electron.

$$V_s[\rho_s] = -\frac{1}{2} \sum_{j=1}^{N} \langle x_j | \nabla_j^2 | x_j \rangle \tag{32}$$

Provided that the density of the real system:

$$\rho = \rho_s = \sum_{j=1}^{N} \sum_{\sigma} \left| x_j(\vec{r}, \sigma) \right|^2 \tag{33}$$

Then, the energy functional of the real system is written as:

$$E[\rho] = T_s[\rho] + J[\rho] + V_{nn} + E_{xc}[\rho] \tag{34}$$

where all the unknown pieces are collected into the exchange-correlation energy

$$E_{xc}[\rho] = E[\rho] - T_s[\rho] - J[\rho] + V_{ee} \tag{35}$$

The main challenge in implementing DFT is to find a good approximation to the exchange-correlation energy functional $E_{xc}[\rho]$. There are various approximations to calculate $E_{xc}[\rho]$, such as Local Density Approximation (LDA) and Generalized Gradient Approximation (GGA).

In the DFT calculation, scientists used the local density approximation (LDA) for the exchange-correlation functional. In this approximation, the local exchange-correlation potential at each position $r$ is the exchange-correlation potential for a homogeneous electron gas at the electron density observed at that position.

$$V_{XC}^{LDA} = V_{XC}^{electron\ gas}\,[n\,(r)] \tag{36}$$

The generalized gradient approximation (GGA) is the second approximations which are used for the exchange and correlation energies in the Kohn-Sham method. In the GGA approximation, the exchange and correlation energies include the local electron density and the local gradient in the electron density.

$$V_{XC}^{GGA} = V_{XC}^{electron\ gas}\,[n\,(r)] \tag{37}$$

### 3.15. WIEN2K Computational Program

It is quite difficult to theoretically calculate the optical and electronic properties of atomic structures. Computer-aided computational programs with different features are

used to overcome this problem. These programs are WİEN2k, ABINIT, SİESTA, Quantum ESPRESSO, VASP etc. are simulation programs.

In this thesis, the WİEN2k program was used to examine pure and Mg-doped ZnO crystal. The WIEN2k (Blaha et al., 2020) program is based on DFT and using augmented plane wave plus local orbitals (APW + lo) to solve the Kohn-Sham equations. Many properties can be calculated such as electronic bandstructure, optimized atomic structure, etc... (Blaha et al., 2020).

It uses the APW (Augmented Plane Wave) method and the LAPW (linearly augmented plane wave) method, which is an extended version of APW. It also incorporates the exchange and correlation energy into the process with the help of PBE-GGA, PBEsol-GGA, WC-GGA and LSDA, which are derivatives of the GGA and LDA approaches.

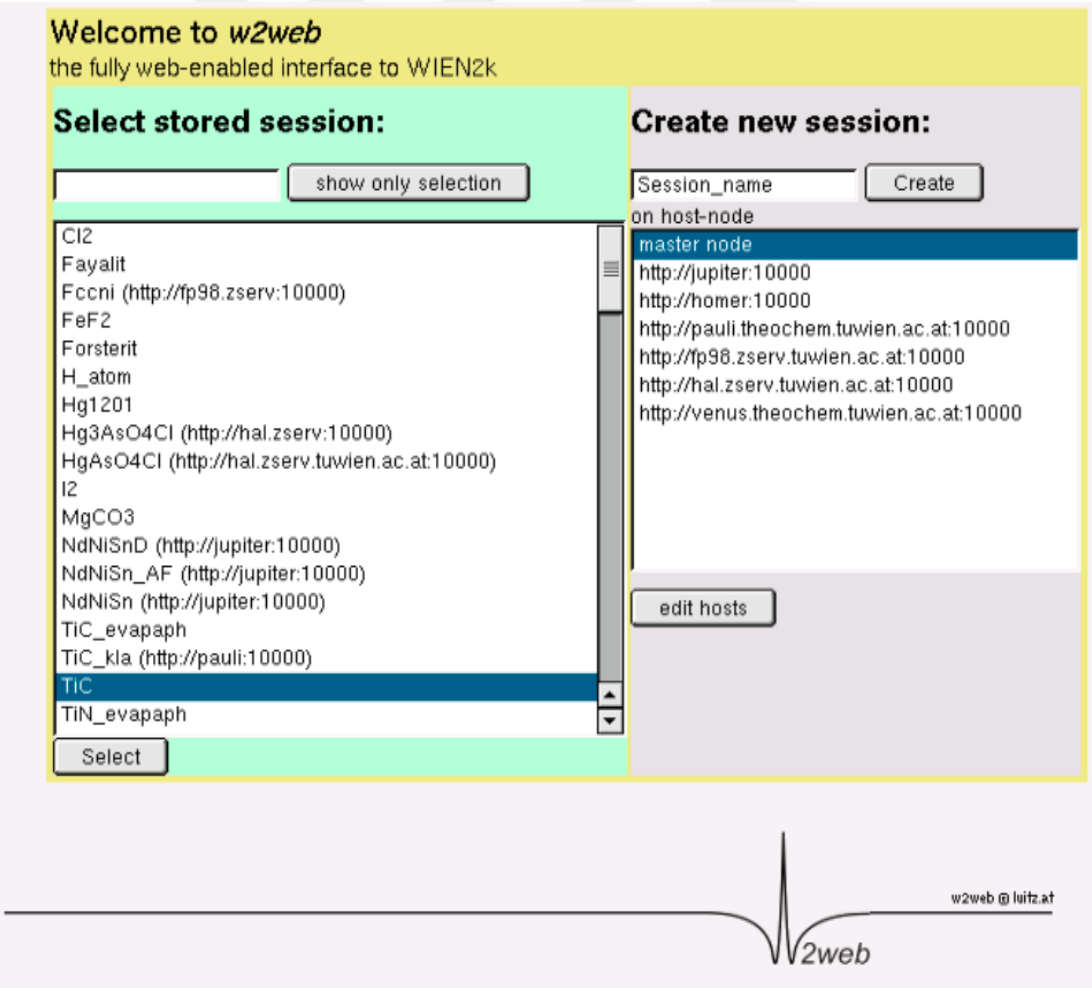


Figure 3.10. The login screen of the WIEN2k computer calculation program.

The input interface of the system is as in Figure (3.10). The "Select stored session" part in the interface is used to reach the work done before, and the second part "Create new session" is used to reach the processes required for the new material to be worked on. The structure file (StructGen) must be created at the start of the program.

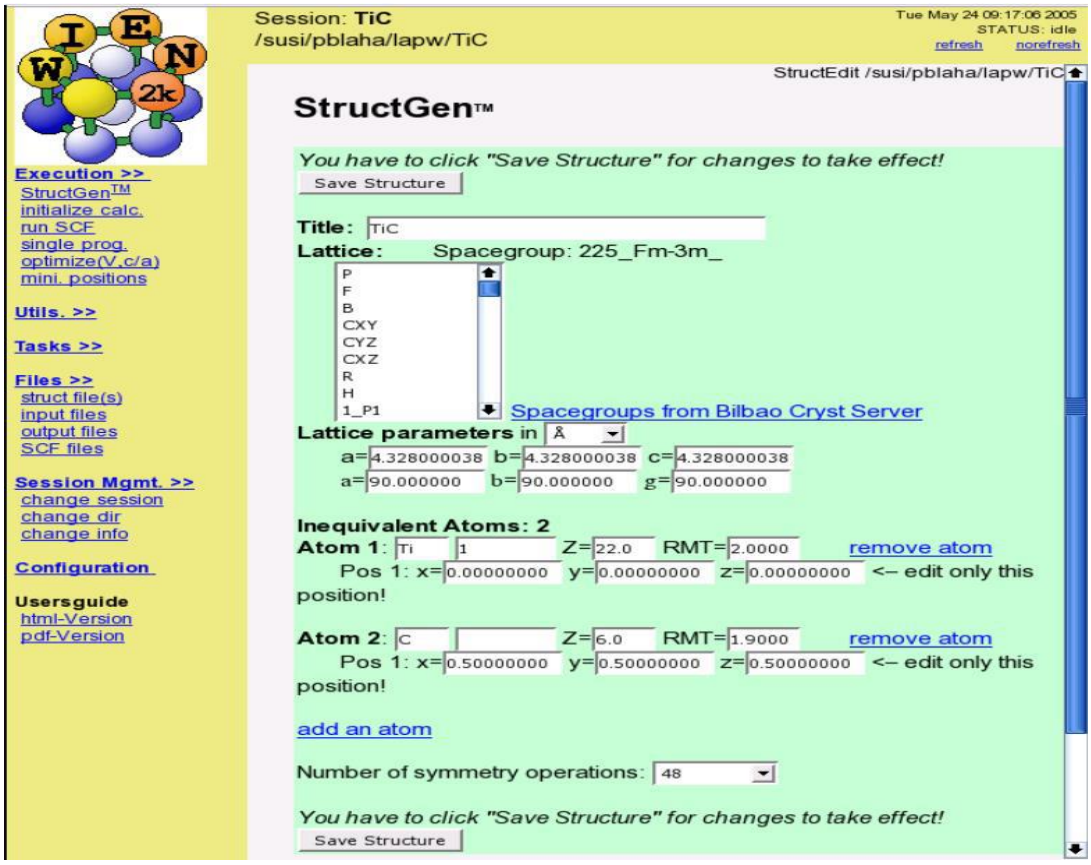


Figure 3.11. The screen on which the atomic positions of the WIEN2k computer program is calculated.

The information belonging to the atom such as the lattice structure of the crystal, lattice parameters, atomic number (Z) and the atom's name in the periodic table is inserted in the relevant places on the screen shown in Figure (3.11).The important thing is that the atoms do not overlap in the unit cell. If the atoms overlap, the system will fail.

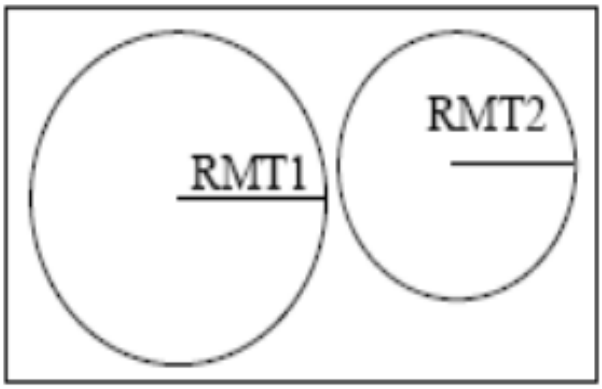


Figure 3.12. The atomic sphere in a unit cell.

*x nn*: Calculates the distance between the closest neighbour atoms (Usually there are 2 adjacent atoms)

*case.output nn*: look at atomic sphere radii (RMT).

*Wiev output nn*: check whether the atomic spheres overlap and whether the number of the second-closest neighbour atoms is correct.

*x sgroup* : This command is struct gen. Uses mesh type, mesh constants, atom positions from the structure file. However, it determines the symmetry points and space group.

*case.outputs group*: Shows space groups.

*x symmetry* : Generates space group symmetry operators in general.

*Instgen lapw* : Allows the definition of the spin polarization of each atom of the structure.

*x lstart* : Generates atomic densities.

The energy value that separates the core and valence electrons is determined. Here it is determined which approach will be used for the exchange and correlation potential energies (PBE-GGA, WC-GGA, PBEsol-GGA and LSDA).The information generated by *view outputst*: *x lstart* is checked.

*Check .in1 st*: APW, LAPW can be changed and larger energy value can be obtained in DOS chart by increasing the value of.

*Check .int2 st*: $Gmax$ value can be reduced or calculated automatically by the system.

Prepare input files: in0, in1, in2, inc and in m files are created and the LM, $Gmax$ and Fermi Energy level is determined.

*x kgen*: The k points and *nkpt* values required in the Brillouin region are produced.

*x list:* Here k points are checked for the irreducible Birilloun region.

At the same time, the energy value can be changed within the first k point.

*x dstart*: The initial density is created for the Self-Consistent Field (SCF) loop, and the program is run using the superposition of atomic densities created by *lstart.View*.

*outputd and cp:* The size of the $Gmax$ and $Gmin$ values are checked.

*case.outputd:* Must be greater than GMAX> GMIN. It is checked from the file. Then it is asked whether spin-polarization will be done or not.

Now all files for the SCF loop are created. "Run_lapw" command is written and executed for SCF (self – consistency cycle). The program makes the following calculations automatically. Convergence criteria are determined on the new screen. SCF cycle,

*LAPWO*: It creates potential from density.

*LAPW1*: Calculates the valence bands.

*LAPW2*: Calculates the valence densities.

*LCORE*: Calculates core states and densities.

# 4. EXPERIMENTAL PROCEDURE

This chapter includes preparing ZnO thin films with co-doped by magnesium and yttrium with different concentration and layers deposited on the bases of the glass substrate by hydrothermal method using Autoclave instrument.

## 4.1. Hydrothermal system

The autoclave machine is made of a cylindrical metal (SS304) in one stainless st eel and has a 200ml Teflon inside, with a resistivity of 100 to 450ºC and a pressure of 3 Mpa. The safe working temperature is up to 280°C and temperature heating and cooling speed is ≤ 5 °C / min. This tool was provided by Company Topton Instrument co, Limited, China and Figure (4.1) shows the thermal pressure system used in my thesis.

Figure 4.1. The image of Autoclave device.

## 4.2. Materials and Method

### 4.2.1. Substrates cleaning process

In our study, minerals and semiconductors were deposited on standard Microscopic slide Glass. In the process of preparing ZnO films with co-doping, the standard glass was used. There are several steps to clean the substrate from the presence of impurities on the surface of the glass substrate which affects the properties of the films. The steps are as follows:

1. The glass substrate was washed with deionized water to get rid of the impurities due to the working environmental condition.
2. The glass substrate is immersed in a fluid which includes acetone, ethanol, and dehydrated water consecutively for 30min. After then, the beaker is placed in the ultrasonic bath to ensure to remove any contaminations present on the surface.
3. The bases are left to be dried
4. Finally, the glass bases are dried with nitrogen gas.

### 4.2.2. Materials

Y and Mg co-doped nanorods of ZnO were prepared by hydrothermal method. The materials used for the preparation of $Zn_{90}Y_xMg_{10-x}O$ where (x= 0, 0.05 and 0.10%) are zinc acetate dihydrate $Zn(CH_3COO)_2{\cdot}2H_2O$ (Sigma Aldrich, 99%), Zinc nitrate hexahydrate $Zn(NO_3)_2.6H_2O$ (Sigma Aldrich, 98%), hexamine $C_6H_{12}N_4$, magnesium nitrate hexahydrate $Mg(NO_3)_2.6H_2O$ (Mark, 98.5%) and Yttrium nitrate hexahydrate $Y(NO_3)_3 \cdot 6H_2O$(Sigma Aldrich, 99%). Also, ethanol absolute, deionized water, 96% ethanol were used as solvents and nitrogen gas was used to clean glass slide which has a substrate on.

## 4.3. Preparation of (ZnO) nanorod by Hydrothermal

### 4.3.1. Preparation of ZnO seed layer

One of the main advantages of using ZnO nanostructures as a seed layer in the hydrothermal growth process is to provide ZnO nanostructures with nucleation sites by decreasing the thermodynamic distance between heterogeneous materials(Zainelabdin et al., 2010). Also, in the final product morphology, the ZnO seed layer was found to be an important element, e.g. orientation and uniformity of the ZnO nanostructure. The preparation of the seed layer, zinc acetate Zn $(CH_3CO_2)_2$ $2H_2O$ has a white colour in shape that dissolved in water and it has molecular weight 219.498g / mol with a melting point of 237°C. Zinc acetate was dissolved in 50 ml of ethanol with a concentration of 10 mM , and the solution was stirred and mixed using the ultrasonic bath for 20 min. the micropipette is used to drop 25 microliters of solution for each $cm^2$ of substrate for producing one layer and glass substrate was placed on a hot plate at a temperature of $55\,°C \pm 5°C$ for dry. This process was repeated 25 times. After then, the fabricated samples are annelated by air at a temperature of 350 °C for 30min, so, the homogeneous seed layer of ZnO has finally obtained. The obtained seed layer is used for processing for secondary rod growth (Kareem, Khodair and Mohammed, 2020). Figure ( 4.2) shows the steps for preparing the seed layer

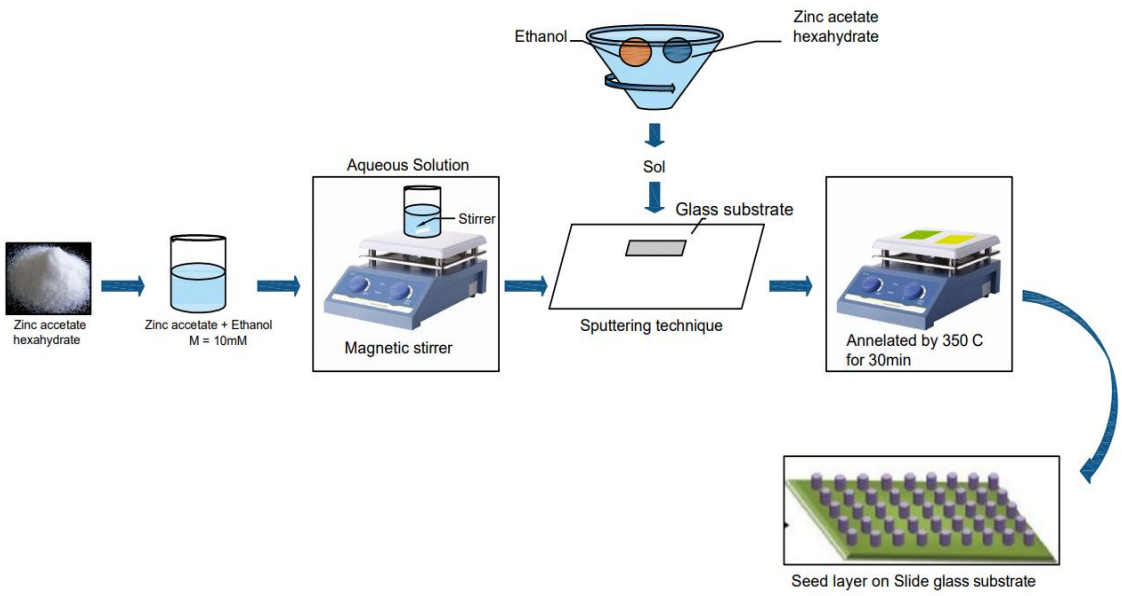


Figure 4.2 Sketch of preparing ZnO seed layers.

### 4.3.2. Growth of ZnO nanorods

The nanorod arrays were prepared from solutions of zinc nitrate hexahydrate $(NO_3)_2.6H_2O$ and hexamethylenetetramine $C_6H_{12}N_4$ on seed glass substrates. 25mM zinc nitrate hexahydrate was dissolved in 50ml of deionized water and solutions were mixed slowly until all sample dissolved inside the solution. Then, the mixture was put inside the ultrasonic machine for 20 min. The same process was repeated for hexamethylenetetramine with 25mM of concentration before adding two mixture for the growing purpose of nanorods. After mixing two solutions, it was put in an ultrasonic. An equimolar solution zinc nitrate hexahydrate and hexamethylenetetramine were prepared in the deionized water and the seed layer substrates were immersed in a solution and fixed in a Teflon up-down position. The growth solution was kept in stainless steel autoclave for 10 hours at 150°C. It was then allowed to cool naturally. After the reaction was complete, the samples were taken out of the oven and washed with deionized water to remove unwanted deposits. The samples left in the air to dry and then placed on a hot plate at a temperature of 300ºC for a period 1/2 hours to grow and homogeneity. Figure (4.3) shows the diagram steps for preparing ZnO nanorods.

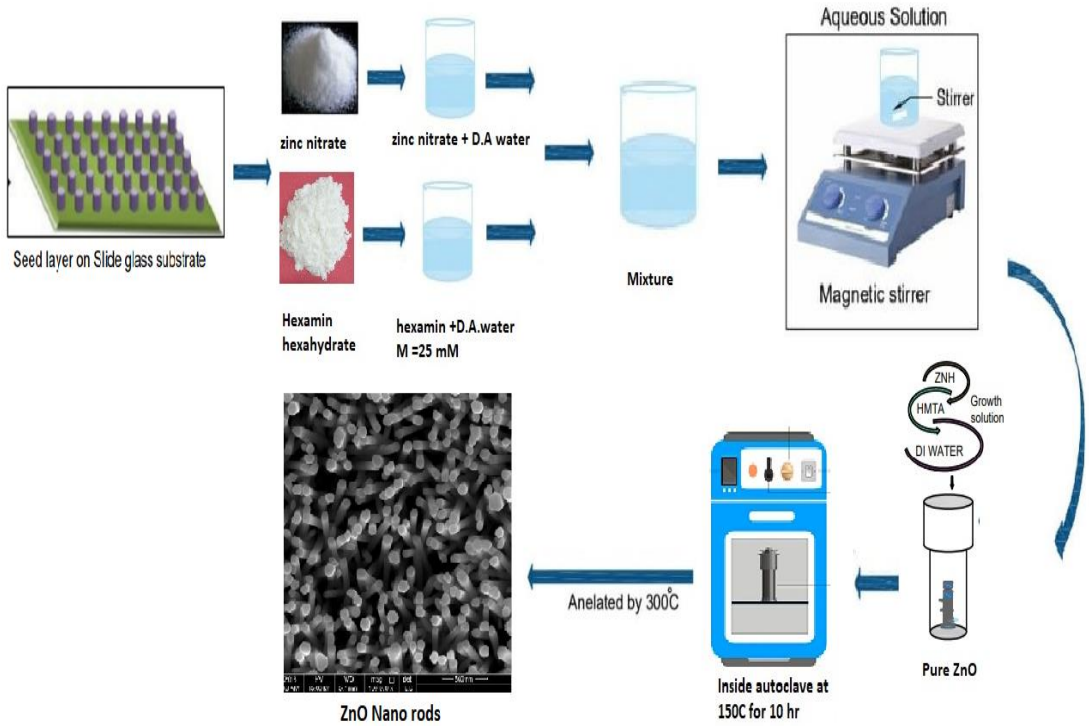


Figure 4.3 Steps for preparing ZnO nanorods.

### 4.3.3. Role of zinc nitrate hexahydrate and hexamethylenetetramine (HTMA)

Zinc nitrate hexahydrate salt provides $Zn^{2+}$ ions which required for building up ZnO nanorods. Also, water molecules in the solution provided $O^{-2}$ ions. Although the exact function of hexamethylenetetramine during the ZnO nanorod growth is still unclear, and it is believed that it acts as a weak base, which hydrolyzes the water slowly and gradually produce $OH^{-}$. However, this reaction is critical in the synthesis process, because if the hexamethylenetetramine hydrolyzes very fast and produces too many $OH^{-}$ions in a short period, then the $Zn^{+2}$ ions in the solution out very quickly due to the high pH environment, which has little contribution to the ZnO nanorod-oriented growth. That means fast consumption of the nutrient and further growth of ZnO nanowires. The above described five chemical reactions could control the growth process of ZnO nanorods:

$$(CH_2)_6N_4 + 2H_2O \leftrightarrow 4NH_3 + 6HCHO$$
$$(NH_3) + H_2O \leftrightarrow NH_3.H_2O$$
$$NH_3.H_2O \leftrightarrow NH_4{}^{+} + OH^{-}$$
$$Zn^{+2} + 2OH^{-} \leftrightarrow Zn(OH)_2$$
$$Zn(OH)_2 \leftrightarrow ZnO + H_2$$

In general, precursor concentration determines the nanowire density. Growth time and temperature control the ZnO nanorod morphology and aspect ratio. Additionally, all of the reactions are actually in equilibrium and can be controlled by adjusting the reaction parameters such as precursor concentration, growth temperature and growth time with pushing the reaction equilibrium forward or backwards. (Zhong Lin Wang, 2011).

### 4.4. Doping process of ZnO

For doping aim, we used zinc nitrate hexahydrate $(NO_3)_2.6H_2O$, magnesium nitrate hexahydrate ($Mg(NO_3)_2.6H_2O$), hexamethylenetetramine (HMT) in the experiment. Firstly, 25mM aqueous solution of Zinc nitrate and 10% Magnesium nitrate were dissolved in 50 ml distilled water by using volumetric ratio. After that, 25mM of HMT was dissolved in 50ml of water. Those solutions were slowly stirring until complete

dissolution. Then, the solution was put in ultrasonic for 20 min. Also, all solutions mixed in one jar and repeat stirring for a complete mixture. The solutions were placed in a Teflon. The bases coated with a seed layer samples was put inside the Autoclave using a thermocouple (Teflon) pillar with a homemade cylindrical design for fixing seed samples, as in figure (4.4). It is important to immerse the sample inside the solution completely. The growth solution was kept in stainless steel autoclave for 10 hours at 150°C. The cooling and cleaning processes which are described above were repeated.

We repeated the above process to obtain Y doped ZnO and Mg-Y co-doped ZnO sample shows in figure(4.6).

Figure 4.4.Image of Teflon base to fix the glass substrates.

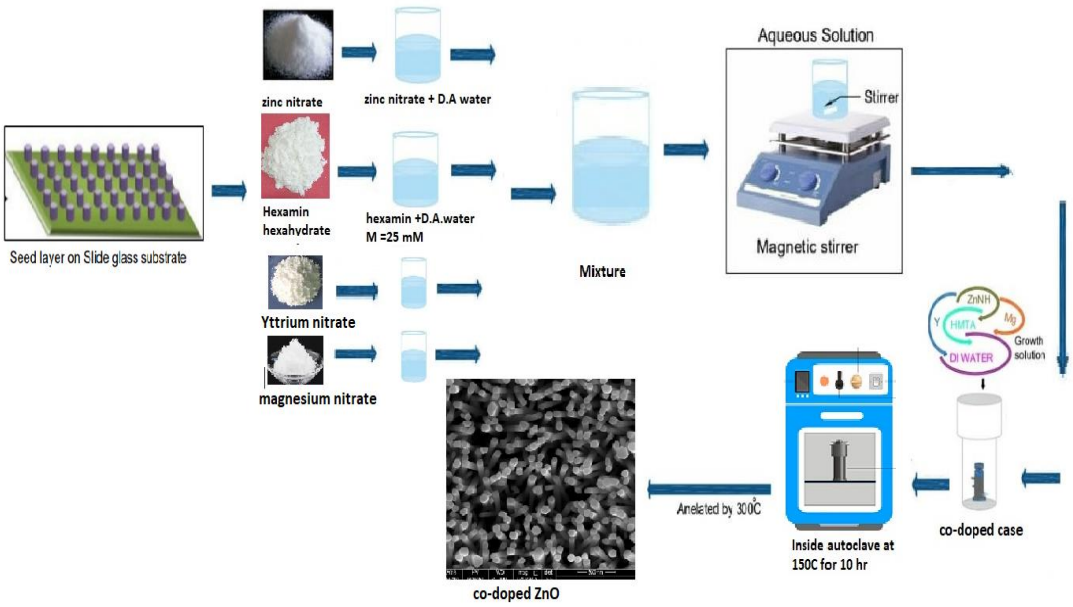


Figure 4.5. Steps for preparing the ($Zn_{90}Mg_{10-x}Y_xO$) films.

# 5. RESULTS AND DISCUSSION

## 5.1. Optical Properties

The optical properties of the pure and $Zn_{90}Y_xMg_{10-x}O$ with $(x = 0\%, 5\%\ and\ 10\%)$ films prepared by the hydrothermal technique. All prepared samples are measured using UV-VIS spectroscopy in the range from 300nm to 900nm to obtain absorbance and transmittance data. The optical energy gap was calculated using the ***Tauc equation***.

### 5.1.1. Absorbance

Absorbance measurements were taken and plotted within the range wavelengths of 300 to 900 nm for pure, doped, and co-doped ZnO. In figure (5.1) shows before and after annealing of the seed layer.

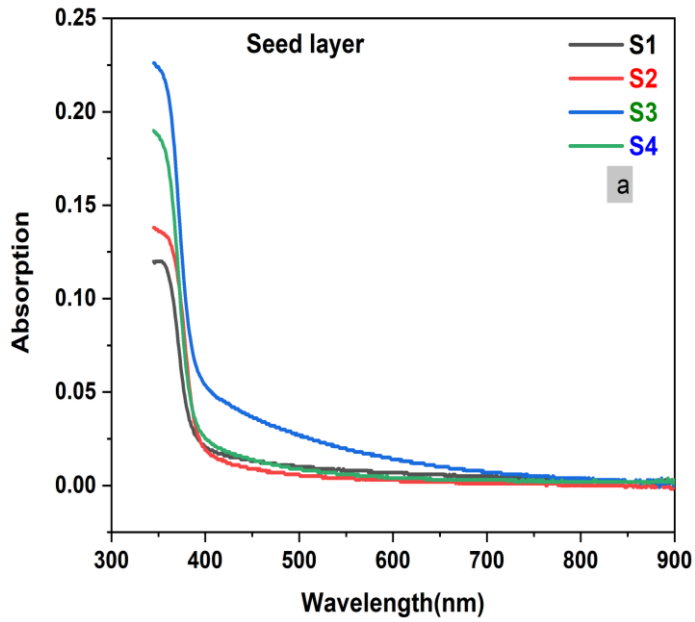


Figure 5.1 The absorbance of the samples in the case (a) seed layer, (b and c) before and after annealing.

We prepared four seed layers which ensure the adherence of the main to the substrate. The figure (5.1a) shows the absorbance of four difference seed layer on samples. As seen from the figure (5.1a) that annealing process does not affect of absorption character of seed layer except sample 4 due to preparing time and environmental condition. All sample shows the same behaviour dependence on wavelength.

It is important to emphasize that the value of the absorbance depends on the size of particles, flaws or defects in grain structure, doping materials and oxygen deficiency.

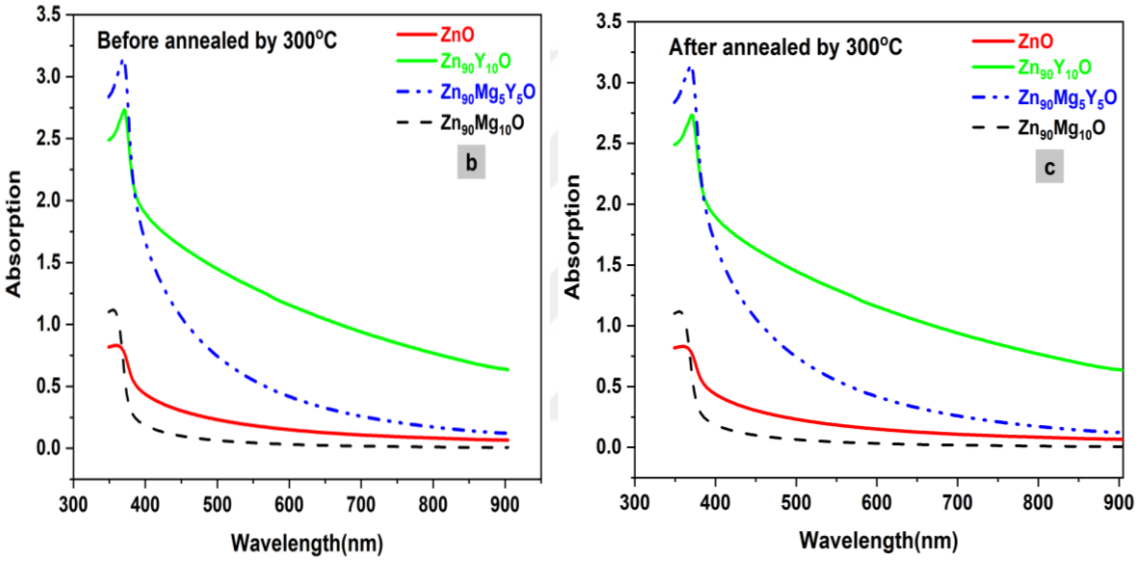


Figure 5.1 The absorbance of the samples in the case (a) seed layer, (b and c) before and after annealing. (continue)

Figure (5.1 b-c) show absorbance data in the case before and after annealing of pure, doped and co-doped samples. As seen in figure (5.1 b-c), absorbance behaviour of samples does not change the before-after annealing process. It means the annealing does not affect the absorbance behaviour of samples after the autoclave process and crystal structure does not change with the annealing process.

In the pure case of ZnO, the red line shows the absorbance was the highest point is 363nm and rapidly decreased in 400nm also gradually decreased from 400 to 700nm and became stable from 700 to 900nm.

ZnO: Y case which represented by the green line, absorbance rapidly decrease from 371nm to 400nm, and a slow decrease from 400nm till 900nm. However, our

measurement limit does not show where the absorbance of the sample gets zero or stable. Also, the result showed that the absorption edge shifts along longer wavelengths. These results agree with other researcher findings (Sagar et al., 2007).

By adding Mg to ZnO which is the blue line, the absorbance decreases rapidly in the range of 355nm to 400nm, and become stable. As seen from the figure that when sample doped with Mg, the data shifts in the absorption edge towards the blue region which reflects the incorporation of Mg in the ZnO lattice that means the optical band gap was enlarged by Mg doping regardless of crystallinity which is in agreement with the report (Kumar et al., 2013).

By adding 5% of Mg and Y to ZnO which is the black line, the absorbance has pike at 366nm and then rapidly decreases at 400nm. Also, the line gradually decreases from 400nm to 700nm. After 700 nm, the absorbance of the sample becomes stable. The result shows that adjusting doping elements into the ZnO sample with a different ratio, the behaviour of absorption also changes.

### 5.1.2. Transmission

The transmittance spectrum is plotted in figure (5.2). The figure shows the transmittance spectrum as a function of the wavelength in the range between 300-900 nm for the case before and after annealed by 300°C. İt is clear that annealing process does not affect the transmission behaviour of the sample as expected.

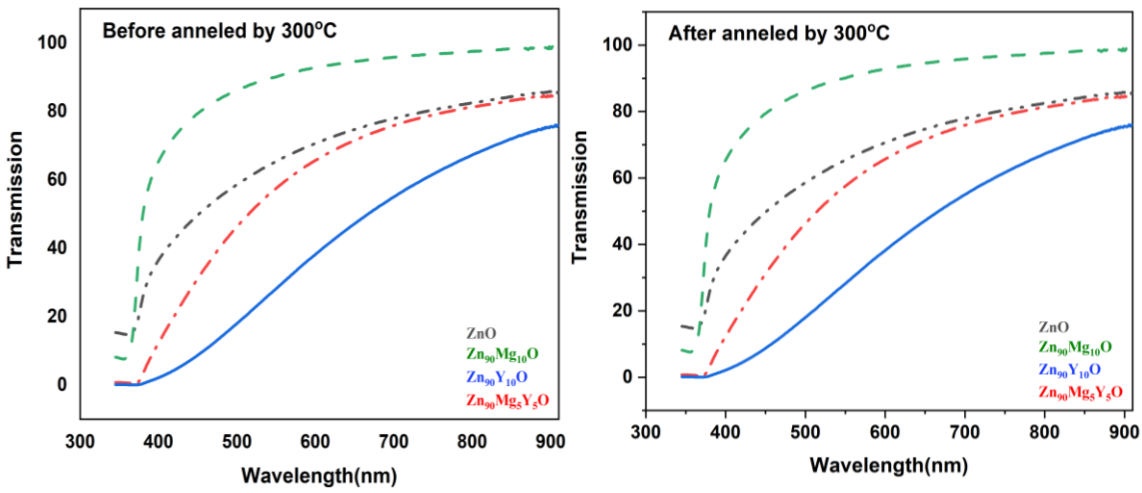


Figure 5.2. The transmittance of the samples for the case before and after annealed by 300°C.

As it appears from the figures, all of the films exhibit higher transmission exceeding about 64 to 90% in the visible region with a fundamental absorption edge.

The pure ZnO film in figure (5.2) shows the low transmittance of the spectral range from λ = 300 to 350 nm and increases rapidly between λ= 350 - 450 nm. The maximum point of transmittance is observed at about 76% in the range of 450 to 550nm. Then it increases slightly from 550nm to 700 and gets stable due to weak absorbability.

In figure (5.2), the green line shows the transmittance study for ZnO doped with Mg. The maximum transmittance is observed about 90% in the range of 360nm to 450nm. and gradually increased from 450 to 600nm, then become stable. This indicates that optical transparency edge changes toward higher photon energies. This result is an agreement with other literature (Huang et al.,2012).

When Yttrium added to ZnO, the transmittance is rapidly increased till 400nm. In addition, the film has highly transparent in range 400 to 550 with a transmittance value of 64 % and this value gradually increases from 550 to 900nm. These results agree with the previous study (Mariappan, 2014).

Additionally, in the case co-doped (Mg, Y) ZnO, the transmittance is increased rapidly 75%. This result between the two above case. This finding also indicates that adding different element in sample affecting transmittance behaviour of the sample.

We also note that the transmittance spectrum exhibits similar visual behaviour as it is in the total Transparent conduction oxides (TCO) ( Jun et al., 2012), which indicates that the films are suitable for solar cell applications because the effective spectral region in the solar cell is in the visible region.

### 5.1.3. Optical energy bandgap

The energy gap depends on the films structure, the arrangement and distribution of atoms in the crystal lattice, and crystal regularity. The previous studies show that ZnO has a direct bandgap transition(Narayanan, 2016). Using this information, the optical energy gap $E_g$ was calculated via Taug equation.

$$(\alpha h\upsilon)^{1/n} = A\left(h\upsilon - E_g\right) \quad (38)$$

where $h$ is Planck's constant, $\upsilon$ is the photon's frequency, $\alpha$ is the absorption coefficient, $E_g$ is the bandgap and A is constant. In our case, n equals to ½ for allowed direct transitions for ZnO thin films. The extrapolation of the straight line to $(\alpha\ h\upsilon\ )^2 = 0$ gives the value of the direct bandgap of the material. The dependence of $(\alpha h\upsilon)^2$on $h\upsilon$ is shown in figure (5.3). From this figure, the obtained $E_g$ values are 3.262 , 3.18 , 3.31, 3.157, 3.07 eV for seed layer, $ZnO$ , $Zn_{90}Mg_{10}O$ , $Zn_{90}Y_{10}O$, and $Zn_{90}Mg_5Y_5O$, respectively.

A bandgap decrease (redshift) with a decrease in crystal size up to the critical value and the bandgap increases below the critical value (blue-shift). Generally, the result showed that how doping affected the energy bandgap.

Figure (5.3a) shows the energy band gap as 3.262 eV for seed layer of ZnO after the annealing process. From figure (5.3b), the energy bandgap for pure ZnO is 3.18 eV after the autoclave techniques. The bandgap value of the sample after the autoclave decreases compared to seed layer bandgap. The behaviour can be explained with the temperature, particle size and modification structure of the film after annealing.

In the case, ZnO: Mg, the bandgap is calculated as 3.31 eV. This bandgap results in good agreement with previous experimental study (Inbaraj et al., 2018). The observed value was shifted to lower wavelength, the reason beyond the shifting might be due to the smaller ionic radius of $Mg^{2+}$ compared to $Zn^{2+}$(Islam et al.,2020). Such an increase in bandgap could be attributed to the Burnstein–Moss effect (Kara et al., 2020)

Y doped ZnO case, the $E_g$is calculated as 3.07 eV(redshifted). This value is lower than the undoped case. This result might be explained as the decrease of the crystalline size and modification of the grain boundary configuration occurred during growth (Kaur, 2004 ).

From figure(5.3e), the energy band gap was observed 3.157eV for $Zn_{90}Mg_5Y_5O$. This value is higher than Y doped ZnO, but, lower than pure and Mg-doped ZnO case. This energy band gap value implies that the effects of Y on the forbidden energy band gap dominate comparing with Mg case. Moreover, this result could be due to the effect of dopant elements yttrium and magnesium on the forbidden energy bandgap

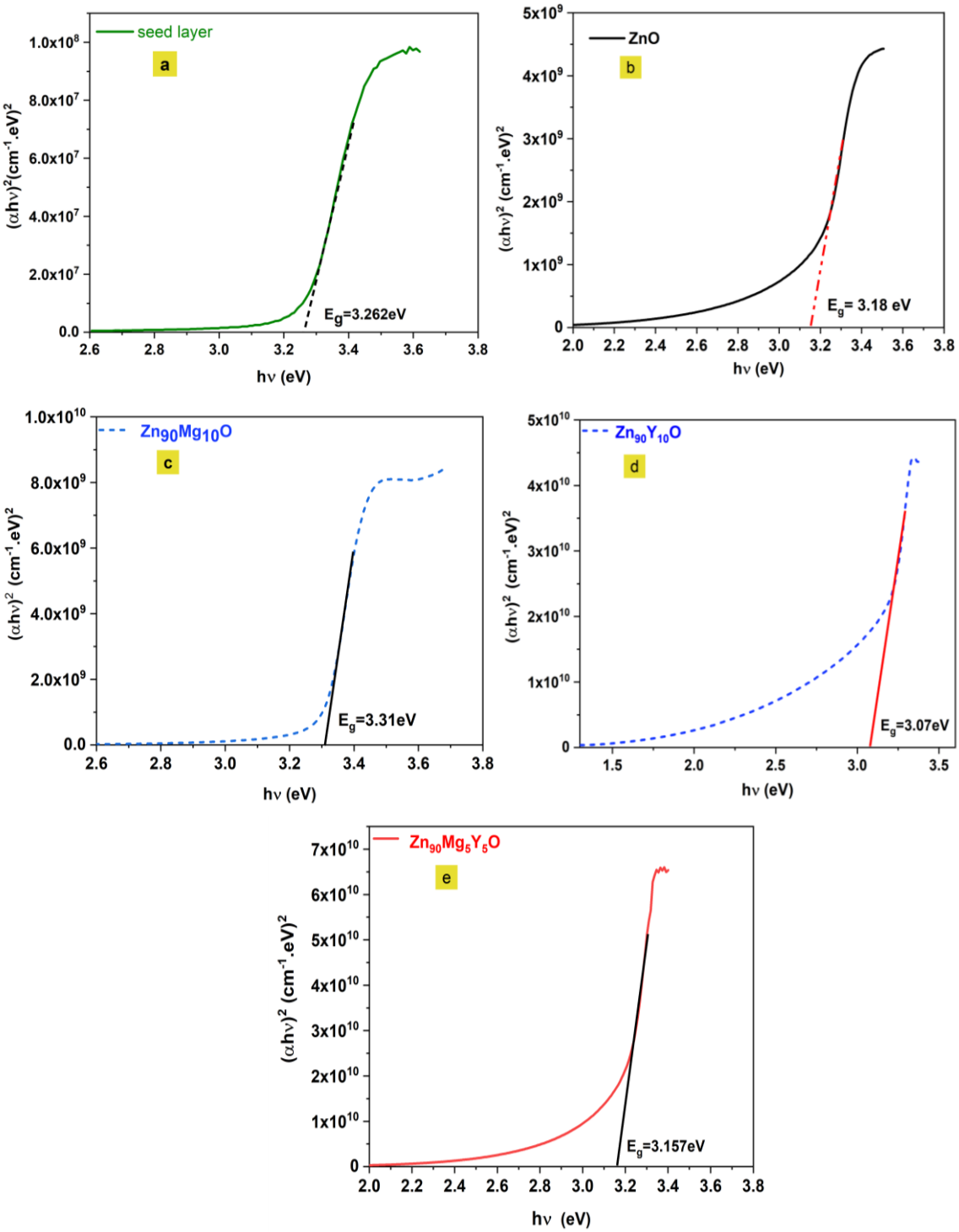


Figure 5.3. The energy bandgap for (a) seed layer, (b)ZnO, (c) $Zn_{90}Mg_{10}O$, (d) $Zn_{90}Y_{10}O$ , (e) $Zn_{90}Mg_5Y_5O$.

## 5.2. Theoretical Study

### 5.2.1. Volume optimize process

The theoretical lattice parameters calculated via using parameters and the total energy-volume, according to the four potentials which are used for exchange-correlation potential in the WİEN2k package program. The minimum values of energy versus volume were examined for four potentials (PBE-GGA, LSDA, WC-GGA and PBEsol-GGA)shows figure(5.4). After applying the Birch-Murnaghan equation (Murnaghan, 1944) fit function, we obtained theoretical the lattice constant. Also,

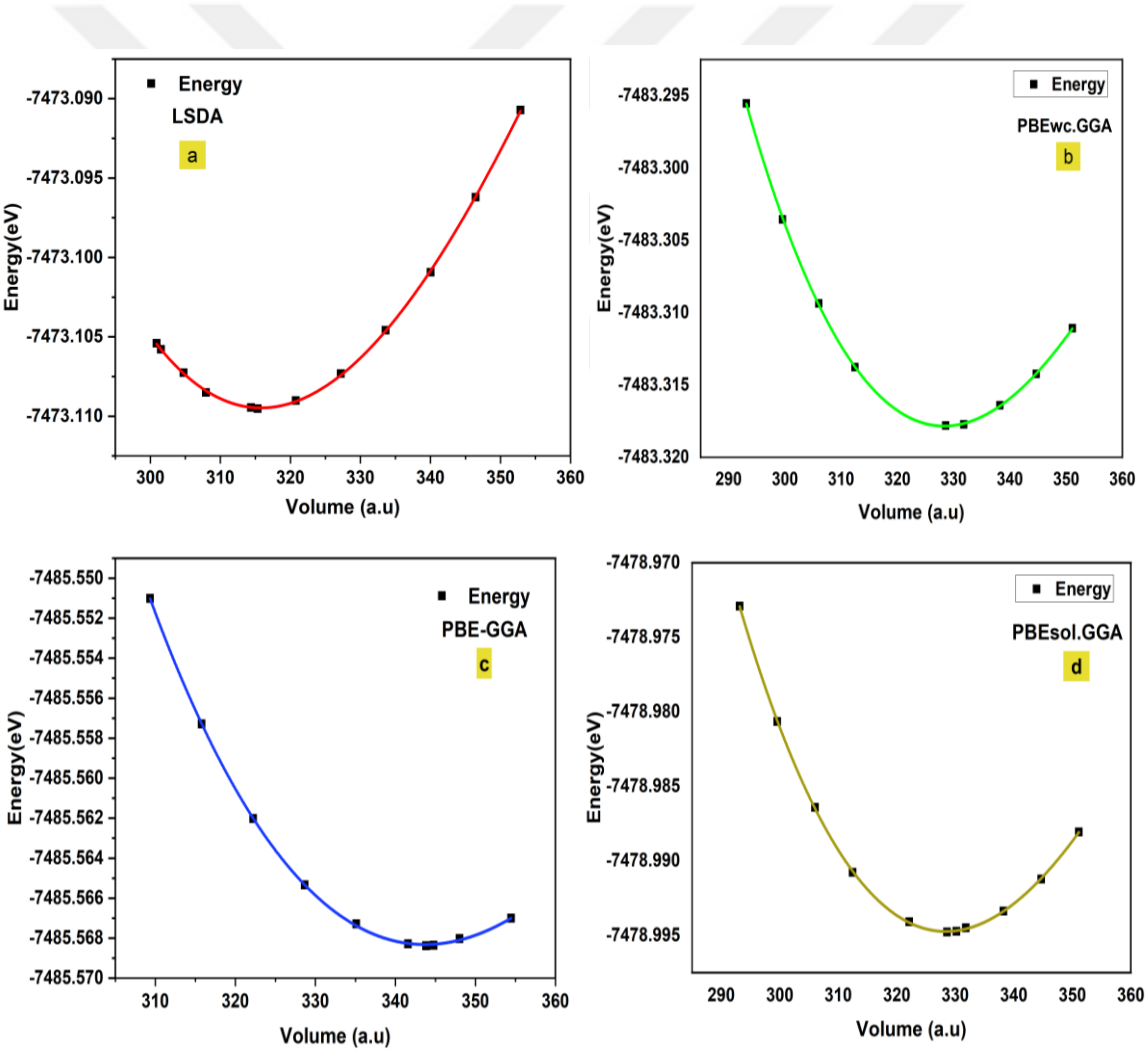


Figure 5.4. Energy (eV) vs. Volume $(a.u)$ plots of ZnO crystal under (a) LSDA, (b) WC-GGA, (c) PBE-GGA, (d) PBEsol-GGA, and (e) PBEsol+hf potentials.

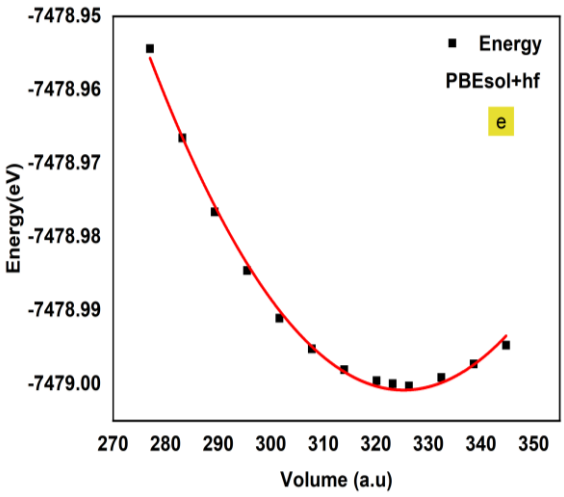


Figure 5.4. Energy (eV) vs. Volume $(a.u)$ plots of ZnO crystal under (a) LSDA, (b) WC-GGA, (c) PBE-GGA, (d) PBEsol-GGA, and (e) PBEsol+hf potentials.(continue)

In Figure (5.4), the theoretical lattice constants for four plus one potentials embedded in wien2k program are determined by minimizing the ratio of total energy to volume. The calculated lattice parameters for all potentials were inserted in the table (5.1) with the experimental lattice constant of ZnO.

Table 5.1. The experimental and lattice parameters of ZnO crystal obtained under PBE-GGA, LSDA, WC-GGA and PBEsol potentials

| Lattice parameter | Experimental | PBE-GGA | LSDA | WC-GGA | PBEsol-GGA | PBEsol+hf |
|---|---|---|---|---|---|---|
| a | 3.24949 | 3.313742 | 3.230981 | 3.274225 | 3.260296 | 3.160746 |
| b | 3.24949 | 3.313742 | 3.230981 | 3.274225 | 3.260296 | 3.160746 |
| c | 5.21999 | 5.322379 | 5.190252 | 5.259718 | 5.237344 | 5.192840 |

There is an inverse proportion between pressure and volume. The pressure decreases as the volume increases. The value where the pressure is zero corresponds to the value where the total energy is stable.

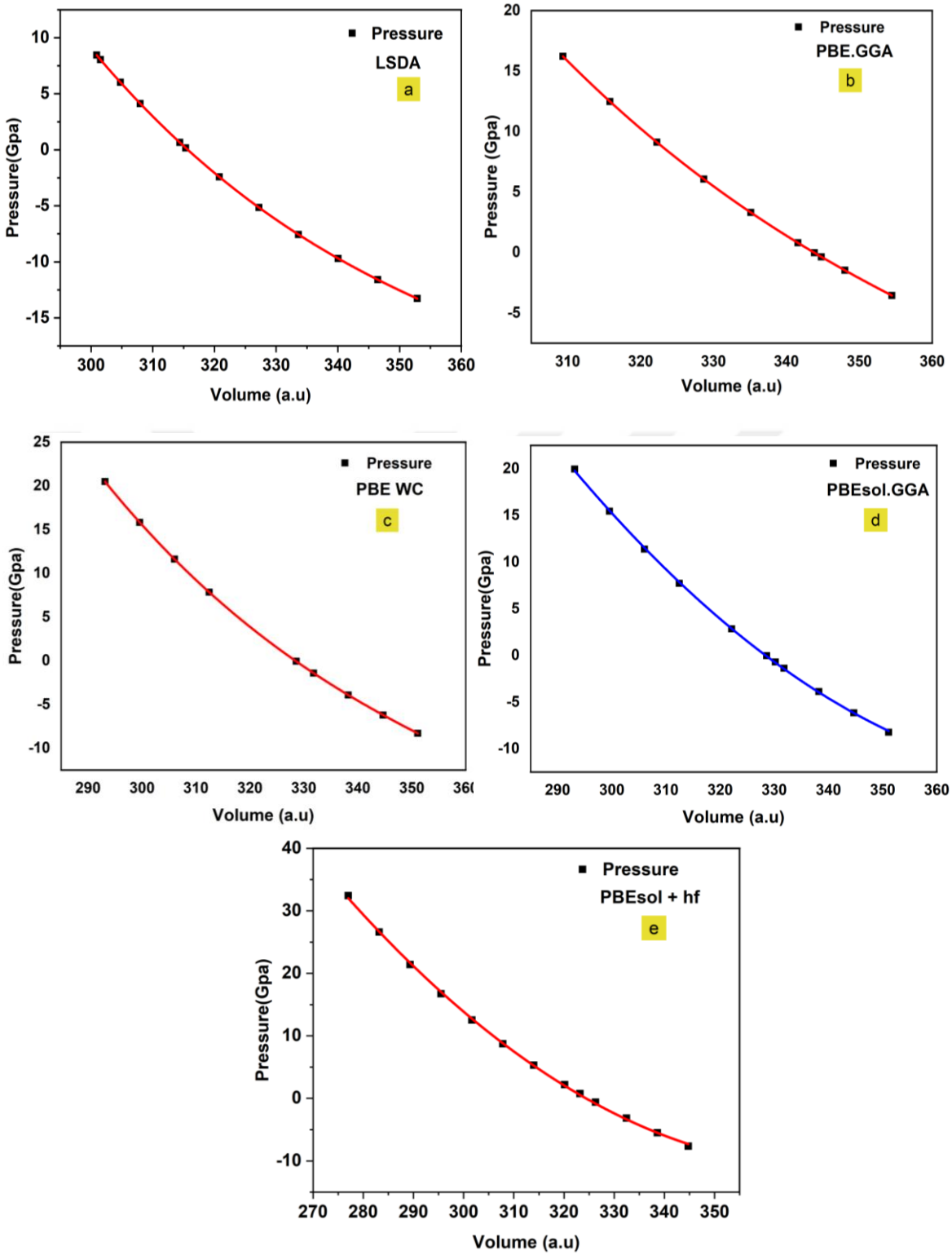


Figure 5.5. Pressure (GPa) vs. Volume (a.u) plots of ZnO crystal under (a) LSDA ,(b) PBE-GGA, (c) WC-GGA, (d) PBEsol,(e) PBEsol+hf Potentials.

And the theoretical lattice constant with PBEsol potential is close to experimental finding. We modified by using PBEsol+hf for getting the best result in the calculation in the case of pure ZnO.

### 5.2.2. Electron density

In this part of the study, the electron density of the ZnO crystal was calculated using the WİEN2k program. These obtained data were drawn with the help of the XCrySDen program in the plane of three dimensions (Figure 5.6).

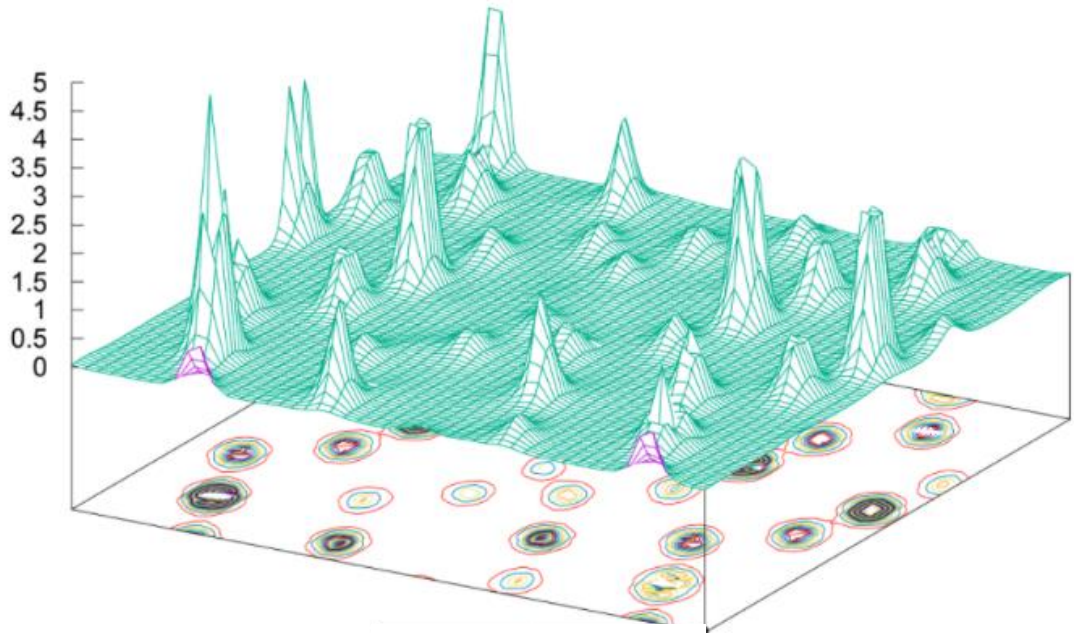


Figure 5.6 Three dimensional electron density for ZnO crystal.

### 5.2.3. Electronic properties of pure and doped ZnO

One of the most investigated characteristics in ZnO is electronic properties. The computed energy band structure and density states reveal the electron features of ZnO. Figure (5.7) displays the electron band structure of zinc blend using PBEsol potential. It can be seen that ZnO has a direct bandgap transition since the top of valance band and bottom of conduction band are located at the same high symmetry point which is gamma.

Figure (5.7) shows the energy band structure between -4 to 8 eV of the energy range It can be observed that forbidden gap energy is 0.67eV for the pure case. The results

are agreement with other researchers studied energy bandgap of ZnO are between 0.64 and 0.813 using in LDA and GGA(Yaakob et al., 2014). And our result is lower than the experimental value due to the nature of GGA which underestimate the binding energy in the d-state resulting in anion p valence hybridization. A strong p-d coupling finally yielded a smaller bandgap. These can be solved by using PBEsol+hf in figure(5.9).

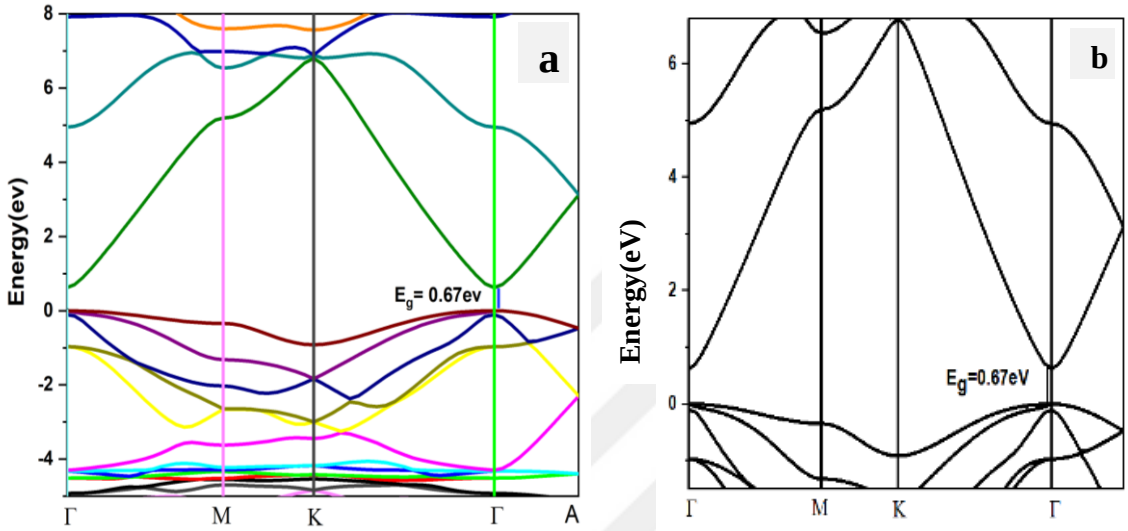


Figure 5.7. The band structure for ZnO, with PBEsol.

Figure (5.8) shows the effect doping on the forbidden bandgap by using PBEsol potential. Mg-doped ZnO is caused to the shift of forbidden bandgap to higher energy value, 0.89eV. This indicates that blue-shifted might be due to the smaller ionic radius of $Mg^{2+}$ (0.78 Å) compared to $Zn^{2+}$(0.83 Å) (Islam et al. 2020). By this reason, the forbidden bandgap is increased.

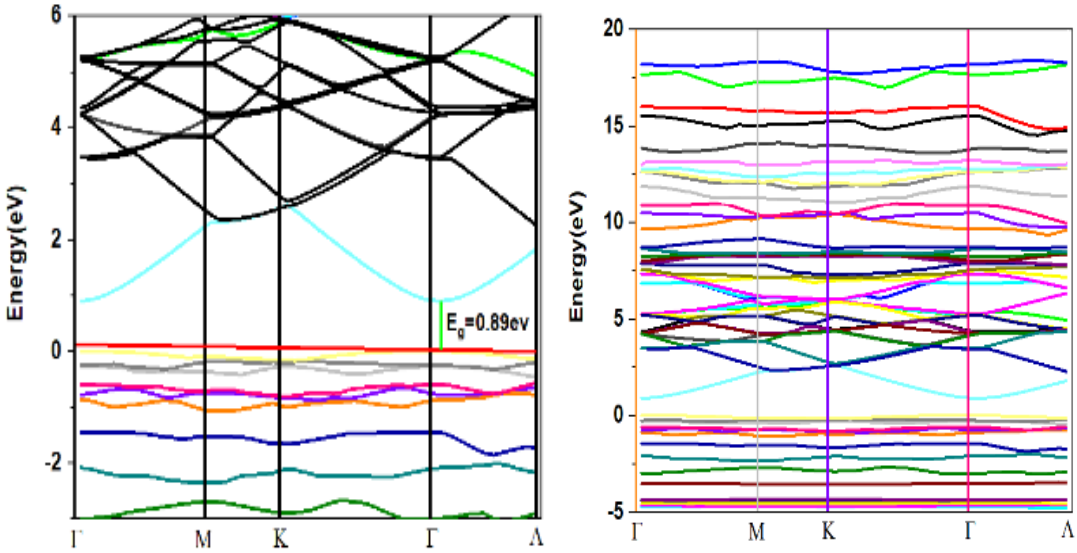


Figure 5.8. The forbidden band structure for ZnO dopped by Mg.

Figure (5.9 ) showed that adding a hybrid function to PBE-sol, the forbidden energy band raises to 2.47eV. this result is more accurate and near to experimental study.

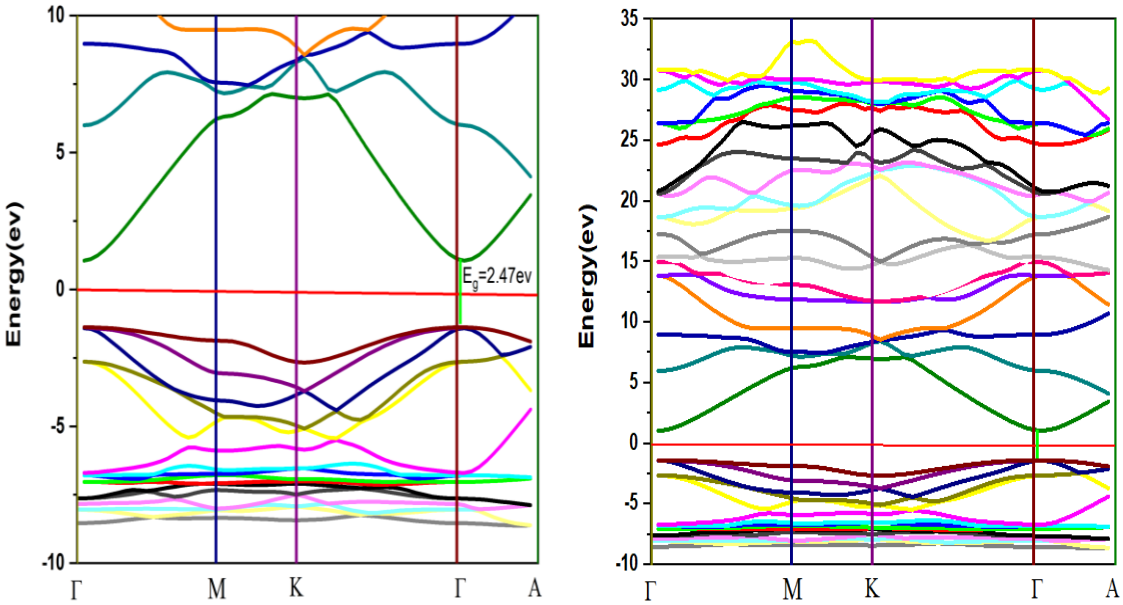


Figure 5.9. The band structure for PBEsol+hf.

## 6. CONCLUSION

Pure, Mg-doped, Y doped, and Mg-Y co-doped ZnO compounds are investigated to determine the effect of the dopping element on the forbidden energy band gap with experimental and theoretical methods.

In the experimental part, the hydrothermal method has been used to prepare samples. Finding results shows that Autoclave techniques do affect data, hovever, annealing temperature does not affect the data. While Mg-doped ZnO sample has absorbance shifted blue region comparing with the pure case, the absorbance of Y, and Mg-Y co-doped ZnO has shifted red region.

In experimental parts, shows that the transition rate of the incoming beam varies with the type of doping element. Mg-doped Zn transmitted at 10% of incoming wave affected lower, but Y doped and Mg-Y co-doped ZnO transmitted part half of the incoming wave light to sample.

As seen from UV-vis measurements, the forbidden bandgap of doped and pure case ZnO has been varied according to the dopping case. Such as in Mg dopped the bandgap is increased and oppositely by doped, Y, and co-doped the forbidden bandgap decreased.

In the theoretical part, we investigated pure and Mg-doped ZnO cases (Due to time limitation, we can not add Y and Mg-Y codoped ZnO sample. We have been still running calculation).

Among the four potential which are embedded in wien2k, PBEsol gave the best theoretical lattice constants which are the closest to experimental findings. However, the value of the forbidden bandgap is small comparing with the experimental result due to the nature of GGA. We rerun our calculation with PBEsol+hf potentials which gave better-forbidden energy band gap value, 2.4 eV. This value is better comparing with experimental results.

We also had Mg-doped ZnO after creating supercell and changed Zn with Mg. Mg-doped ZnO sample has 0.89 eV value for a forbidden energy bandgap. This value is higher than the pure case. This implies that doping ZnO with Mg effects forbidden

energy bandgap due to the smaller ionic radius of $Mg^{2+}$ (0.78 Å) compared to $Zn^{2+}$ (0.83 Å).

## REFERENCES


Akkuş, H., 2007. ***Electronic and Optical Properties of SbSI Crystal: Application of Density Functional Theory***, (Doctoral dissertation). CU, Institute of science, Adana.

Al-Harbi, T., 2011. Hydrothermal synthesis and optical properties of Ni-doped ZnO hexagonal nanodiscs, ***Journal of Alloys and Compounds***, **509**(2): 387-390.

Bakr, N., Salman, S., Shano, A., 2015. Effect of co-doping on structural and optical properties of NiO thin films prepared by chemical spray pyrolysis method, ***International Letters of Chemistry, Physics and Astronomy***, **41**: 15-30.

Barrett, C. S, CS, B., TB, M., 1980. ***Structure of Metals. Crystallographic Methods, Principles and Data***, **35**: 669, Bibl. Dissem.

Baruah, S., Dutta, J., 2009. Effect of seeded substrates on hydrothermally grown ZnO nanorods, ***Journal of Sol-gel Science and Technology,*** **50**(3): 456.

Blaha, P., Schwarz, K., Tran, F., Laskowski, R., Madsen, G. K., & Marks, L. D.,2020. WIEN2k: An APW+ lo program for calculating the properties of solids. ***The Journal of Chemical Physics***, **152**(7):74-101.

Callister, W. D., & Rethwisch, D. G., 2011. ***Materials Science and Engineering***. 5: 344-348. NY: John Wiley & Sons.

Cardona, M., Peter, Y. Y., 2005. ***Fundamentals of Semiconductors***, Springer -Verlag Berlin Heidelberg.

Choi, J. W., Lee, C. M., Park, C. H., Lim, J. H., Park, G. C., Joo, J., 2019. Effect of annealing temperature on the morphology and electrical property of hydrothermally-grown ZnO nanorods/p-Si heterojunction diodes, ***Journal of Nanoscience and Nanotechnology***, **19**(3): 1640-1644.

Chopra, K. L., 1979. ***Thin Film Phenomena***, R. E. Krieger publishing company.

Chopra, K., 2012. ***Thin Film Device Applications***, Springer science and business media. USA.

Debnath, T., Das, S., Das, D., & Sutradhar, S. 2017. Optical, magnetic and dielectric properties of ZnO: Y nanoparticles synthesized by hydrothermal method. ***Journal of Alloys and Compounds***, **696**: 670-681.

Djurišić, A. B., Leung, Y. H., 2006. Optical properties of ZnO nanostructures, ***Small***, **2**(8): 944-961.

Duman, U., 2020. ***Investigation of Electronic and Optical Characteristics of CaNb2O6 Compound at Room Temperature***. (Master thesis) Van Yüzüncü Yıl Univ. Institute of science. Van.

Ece, N., 2017. ***Investigation of Physical Properties of BiRhO3 Crystal by DFT***. (Master thesis) Van Yüzüncü Yıl Univ. Institute of science. Van.

Ferreira, L. G., Marques, M., Teles, L. K., 2008. Approximation to density functional theory for the calculation of band gaps of semiconductors, ***Physical Review B***, **78**(12): 116-125.

Feynman, R. P.,1960. ***There's Plenty of Room at the Bottom***, California institute of technology, engineering and science magazine,

Foo, K. L., Hashim, U ., Muhammad, K., Voon, C. H., 2014. Sol-gel synthesized zinc oxide nanorods and their structural and optical investigation for optoelectronic application, **Nanos*cale Research Letters***, **9**(1): 429.

Fox, M., 2001. ***Optical Properties of Solids***, OUP Oxford.
Fox, M., 2002. ***Optical properties of solids***, American association of physics teachers.
Freund, L. B., Suresh, S., 2004. ***Thin-film Materials: Stress, Defect Formation and Surface Evolution***, Cambridge university press.
Goldstein, J. I., Newbury, D. E., Michael, J. R, Ritchie, N. W., Scott, J. H. J., Joy. D. C., 2017. ***Scanning Electron Microscopy and X-ray Microanalysis***, 4th Edition, New York: Springer.
Haas. G, Thun, R., 1966. ***Physics of Thin Films,*** **3**(3):337 Academic Press, New York.
Huang, K., Tang, Z., Zhang, L., Yu, J., Lv, J., Liu, X., & Liu, F. 2012. Preparation and characterization of Mg-doped ZnO thin films by sol-gel method**.** ***Applied Surface Science***, **258**(8):3710-3713.
Ilican, S., Caglar, Y., Caglar, M., 2008. Preparation and characterization of ZnO thin films deposited by sol-gel spin coating method, ***Journal of Optoelectronics and Advanced Materials***, **10**(10): 2578-2583.
Inbaraj, P. F. H., Prince, J. J. 2018. Optical and structural properties of Mg-doped ZnO thin films by a chemical bath deposition method. ***Journal of Materials Science: Materials in Electronics***, **29**(2): 935-943.
Islam, M. R., & Azam, M. G. 2020. Enhanced photocatalytic activity of Mg-doped ZnO thin films prepared by sol-gel method. ***Surface Engineering***, 1-9.
Jun, M. C., Park, S. U., & Koh, J. H. (2012). Comparative studies of Al-doped ZnO and Ga-doped ZnO transparent conducting oxide thin films. ***Nanoscale research letters***, **7**(1): 1-6.
Kara, R., Mentar, L., Azizi, A. 2020. Synthesis and characterization of Mg-doped ZnO thin-films electrochemically grown on FTO substrates for optoelectronic applications. ***RSC Advances***, **10**(66): 40467-40479.
Kareem, M., Khodair, Z., Mohammed, F., 2020. Effect of annealing temperature on structural, morphological and optical properties of ZnO nanorod thin films prepared by hydrothermal method, ***Journal of Ovonic Research***, **16**(1): 53-61.
Karzel, H., Potzel, W., Köfferlein, M., Schiessl, W., Steiner, M., Hiller, U., Kalvius, G., Mitchell, D., Das, T., Blaha, P., 1996. Lattice dynamics and hyperfine interactions in ZnO and ZnSe at high external pressures, ***Physical Review B***, **53**(17): 114-125.
Khuili, M., Fazouan, N., Abou El Makarim, H., Atmani, E. H., & Houmad, M. (2020). Improvement of optical properties of Mg-doped ZnO by nanostructuring for applications in optoelectronics. ***Materials Research Express***, **7**(2): 025 - 043.
Kittel, C., McEuen, P., McEuen, P.,1996. ***Introduction to Solid State Physics,*** 8:105-130. New York: Wiley.
Klingshirn, C., 2007. ZnO: Material, physics and applications, ***Chem Phys Chem***, **8**(9): 782-803.
Kumar, P., Malik, H. K., Ghosh, A., Thangavel, R., Asokan, K., 2013. Bandgap tuning in highly c-axis oriented Zn1− xMgxO thin films, ***Applied Physics Letters***, **102**(22): 221-303.
Liu, B., Zeng, H. C., 2003. Hydrothermal synthesis of ZnO nanorods in the diameter regime of 50 nm. ***Journal of the American Chemical Society***, **125**(15): 4430-4431.

Liu, H., Chin, T., Lai, L., Chiu, S., Chung, K., Chang, C., Lui, M., 1997. Hydroxyapatite synthesized by a simplified hydrothermal method, ***Ceramics International***, **23**(1): 19-25.

Mariappan, R., Ponnuswamy, V., Bose, A. C., Suresh, R., Raghavendra, M. 2014. Influence of Y doping concentration on the properties of nanostructured $M_xZn_{1-x}O$ (M= Y) thin film deposited by nebulizer spray pyrolysis technique. ***Journal of Physics and Chemistry of Solids***, ***75***(9), 1033-1040.

Mazhdi, M., Hossein, K. P., 2012. Structural characterization of ZnO and ZnO: Mn nanoparticles prepared by reverse micelle method, ***International Journal of Nano Dimension***, **2**(8): 233-240.

Mondal, S., Kanta, K., Mitra, P., 2008. Preparation of Al-doped ZnO (AZO) thin film by Silar. ***Journal of Physical Science***, **12**: 221-229

Moses Ezhil Raj, A., Nehru, L., Jayachandran, M., Sanjeeviraja, C., 2007. Spray pyrolysis deposition and characterization of highly (100) oriented magnesium oxide thin films, ***Crystal Research and Technology: Journal of Experimental and Industrial Crystallography***, **42**(9): 867-875.

Mote, V., Purushotham, Y., Dole, B., 2012. Williamson-Hall analysis in estimation of lattice strain in nanometer-sized ZnO particles, ***Journal of Theoretical and Applied Physics***, **6**(1): 6-25.

Muchuweni, E., Sathiaraj, T., Nyakotyo, H., 2018. Effect of annealing on the microstructural, optical and electrical properties of ZnO nanowires by hydrothermal synthesis for transparent electrode fabrication, ***Materials Science and Engineering: B***, **227**: 68-73.

Narayanan, G. N., Ganesh, R. S., & Karthigeyan, A., 2016. Effect of annealing temperature on structural, optical and electrical properties of hydrothermal assisted zinc oxide nanorods. ***Thin Solid Films***, **598**: 39-45.

Neamen, D. A., 2003. ***Semiconductor Physics and Devices: Basic Principles***. 4th edition, Newyork: McGraw-Hill.

Ohring, M., 2001. ***Materials Science of Thin Films***. Elsevier.

Okada, T., Agung, B., Nakata, Y., 2004. ZnO nanorods synthesized by nano-particle-assisted pulsed-laser deposition, ***Applied Physics A***, **79**(4-6):1417-1419.

Othman, M. S. D., 2009. ***Investigation of Electronic, Elastic and Optical Properties of Some Semiconductors by AB inito Method***. (Doctoral dissertation) Gazi University. institute of science. Ankara.

Özgür, Ü., Alivov, Y. I., Liu, C., Teke, A., Reshchikov, M., Doğan, S., Avrutin, V., Chos. J., Morkoç, H., 2005. A comprehensive review of ZnO materials and devices, ***Journal of Applied Physics***, **98**(4): 4-11

Pankove, J. I., 2012. ***Optical Processes in Semiconductors***, Dover publications. New York: Mineola.

Periasamy, C., Prakash, R., & Chakrabarti, P. 2010. Effect of post-annealing on structural and optical properties of ZnO thin films deposited by vacuum coating technique. ***Journal of Materials Science: Materials in Electronics***, **21**(3): 309-315.

Pillai, S., 2008. ***Modern Physics and Solid-State Physics (Problems and Solutions)***, New international.

Piticescu, R. R., Piticescu, R. M., Monty, C. J., 2006. Synthesis of Al-doped ZnO nanomaterials with controlled luminescence, ***Journal of the European Ceramic Society***, **26**(7): 2979-2983.

Prabhu, Y. T., Rao, K. V., Kumar, V. S. S., Kumari, B. S., 2014. X-ray analysis by Williamson-Hall and size-strain plot methods of ZnO nanoparticles with fuel variation. ***World Journal of Nano Science and Engineering***, **4**(1): 1-8.

Sagar, P., Shishodia, P., Mehra, R., Okada, H., Wakahara. A Yoshida, A., 2007. Photoluminescence and absorption in sol–gel-derived ZnO films, ***Journal of Luminescence***, **126**(2): 800-806.

Sanjeev, S., & Kekuda, D. 2015. Effect of annealing temperature on the structural and optical properties of zinc oxide (ZnO) thin films prepared by a spin coating process. In ***IOP Conference Series: Materials Science and Engineering*** **73**(1): 012-149

Shakti, N., Kumari, S., & Gupta, P. S. 2011. Structural, optical and electrical properties of ZnO nanorod array prepared by hydrothermal process. ***J Ovonic Res***, **7**: 51-59.

Shan, F., Shin, B., Jang, S., Yu, Y., 2004. Substrate effects of ZnO thin films prepared by PLD technique, ***Journal of the European Ceramic Society***, **24**(6): 1015-1018.

Steiner, S. L. M., Hiller, U., Kalvius, G., Mitchell, D., Das, T., Blaha, P., 1996. Lattice dynamics and hyperfine interactions in ZnO and ZnSe at high external pressures, ***Physical Review B***, **53**(17): 114-125.

Thetford, A., 1966. ***Physics of Thin Films***, II, Edited by G. Hass and R. Thun. ConPh, **7**(2): 240.

Varshni, Y. P, 1967. Temperature dependence of the energy gap in semiconductors, ***Physica***, **34**(1): 149-154.

Wang, H., Yuan, X., Zeng, G., Wu, Y., LiuY., Jiang, Q., Gu, S., 2015. Three-dimensional graphene-based materials: Synthesis and applications from energy storage and conversion to the electrochemical sensor and environmental remediation, ***Advances in Colloid and Interface Science***, **221**: 41-59.

Wang, Z. L., 2011. ***Nanogenerators for Self-powered Devices and Systems***, Georgia institute of technology.

Wu, H., Xue, M., Ou, J., Wang, F., & Li, W. 2013. Effect of annealing temperature on surface morphology and work function of ZnO nanorod arrays. ***Journal of Alloys and Compounds***, **565**: 85-89.

Yim, K. G., Kim, M. S., Kim, S., LeemJ.Y., Nam, G., Jeon, S. M., Lee, D. Y., Kim, J.S, Lee, J.I., 2012. Effects of post-annealing temperature on the properties of ZnO nanorods grown on homogenous seed-layers by using the hydrothermal method, ***Journal of the Korean Physical Society***, **60**(10): 1605-1610.

Yogamalar, R., Srinivasan, R., Vinu, A., Ariga, K., Bose, A. C., 2009. X-ray peak broadening analysis in ZnO nanoparticles, ***Solid State Communications***, **149**(43):1919-1923.

Zainelabdin, A., Zaman, S., Amin, G., Nur, O., Willander, M., 2010. ***Deposition of Well-Aligned ZnO Nanorods At 50 C On Metal, Semiconducting Polymer, and Copper Oxides Substrates and Their Structural and Optical Properties***, Crystal growth and design, **10**(7): 3250-3256.

Zhang, X., Sun, W., Kosyachenko, L., Zhang, L., 2008. Temperature dependence of the energy bandgap of HgInTe, ***Infrared Physics and Technology***, **51**(3): 256-258.

**EXTENDED TURKISH SUMMARY**
**(GENİŞLETİLMİŞ TÜRKÇE ÖZET)**

# ZnO'NUN YASAK BANT GAP DEĞERİ ÜZERİNDEKİ DOPİNG ETKİLERİNİN İNCELENMESİ: DENEYSEL VE KURAMSAL ÇALIŞMALAR

MAJEED, Mahmood Hameed
Yüksek Lisans Tezi, Fizik Anabilim Dalı
Tez Danışmanı: Doç. Dr. Murat AYCİBİN
Ocak 2020, 65 Sayfa

## ÖZET

Tez çalışmamızda, deneysel ve teoretik yöntemler kullanılarak zink oksit bileşiğinin yasak enerji bant aralığının katkı maddesi ile nasıl değiştiğini inceledik. Katkı elementleri olarak Mg, Y ve Mg-Y eş katkılı olarak kullanıldı.

Deneysel kısımda, Autoclave methodu, hidrotermal tekniği bir türü, kullanılarak katkılı örnekler elde edildi. Bu kısımda kullanılan autoclave metodondan sonra yapılan tavlamanın, hazırlanan örneklerin soğurma sonuçlarında bir etkisi olmadığı görüldü.

Soğurma grafikleri bize, katkı malzemesine bağlı olarak örneklerin soğurma grafiklerinin farklı olduğunu söylemektedir. ZnO bileşiği Mg ile katkılandığı zaman, soğurma mavi bölgeye kayarken, Y veya Mg-Y ile katkılandığı zaman soğurmanın kırmızı bölgeye kaydığı görülmüştür. Geçirme grafiği ise soğurma grafiğinin onaylayacak şekildedir.

Teorik kısımda, supercell oluşturulup, oluşturulan bu supercell de bir veya iki tabe Zn elementi, katkılanacak durumu göre, Mg, Y veya Mg-Y ile yerdeğiştirlmiştir. Bu şekilde elde edilen örneklerin yasak enerji bant yapılarındaki değişmeye bakılmıştır.

**Anahtar kelimeler:** Yasak bant aralığı, Wien2k, Hidrotermal yöntem, Otoklav, Optik özellikler.

# 1. MALZEMELER VE YÖNTEM

## 1.1 Hidrotermal Sistem

Hidrotermal teknik düşük maliyetli, ve düşük sıcaklıkta süreci kontrol etmemizi sağlayan kolay bir yöntemdir. Her türlü inorganik ve seramik malzeme hidrotermal yöntemle büyütülebilir. Ayrıca, bu yöntem çevre için güvenlidir. Autoclave yöntemi, bir paslanmaz çelik silindir metal (SS304), metal içinde 200 ml Teflon kaplanmıştır. Bu teflon 450$^{o}$C sıcaklık ve 3 Mpa da 100 Ω direnc'e sahiptir. Güvenli çalışma sıcaklığı 280°C'ye kadar çıkabilmekte ve sıcaklık ısıtma ve soğutma hızı ise ≤ 5°C/dak. Bu araç Company Toption Instrument co, Limited, Çin tarafından sağlanmıştır ve Şekil (1.1), tez de kullanılan termal basınç sistemini göstermektedir.

Şekil 1.1 Otoklav cihazının görüntü bölümleri.

## 1.2 Material

Tüm reaktifler ve çözücüler analitik derecedeydi ve daha fazla saflaştırılmadan kullanıldı. Çinko asetat $Zn\,(CH_3COO)_2\,.\,(H_2O)_2$ , çinko nitrat, heksamin $C_6H_{12}N_4$, magnezyum nitrat heksahidrat Mg $(NO_3)_2$ .6($H_2O$) , Yitriyum nitrat hekzahidrat $Y(NO_3)_{\ 3}\,6H_2\,O$, mutlak etanol, deiyonize su, kayar cam substrat, temizleme için % 96 etanol, nitrojen gazı, ultrasonik. ZnO'nun Y ve Mg ortak katkılı nanorodları hidrotermal yöntemle hazırlandı. ( $Zn_{90}Y_xMg_{10-x}O$) O'nun hazırlanmasında kullanılan malzemeler

burada (x = 0, 0.05 ve 0.10) çinko asetat dihidrat $Zn(CH_3COO)_2 \cdot 2H_2O$ (Sigma Aldrich, 99% ), Çinko nitrat heksahidrat $Zn(NO_3)_2.6H_2O$ (Sigma Aldrich,% 98), heksamin $C_6H_{12}N_4$,, magnezyum nitrat heksahidrat $Mg(NO_3)_2.6H_2O$ (Mark,% 98.5) ve Yitriyum nitrat heksahidrat $Y(NO_3)_3 \cdot 6H_2O$ (Sigma Aldrich,% 99). Ayrıca çözücü olarak etanol, deiyonize su,% 96 etanol ve üzerinde substrat bulunan cam slaytı temizlemek için nitrojen gazı kullanıldı.

## 1.3 Hazırlık Tohum Katmanı ve Büyüme ZnO Nano Çubuklar Daldırma Kutusu İle.

Çinko asetat dehidrat, 15 dakika boyunca manyetik sürekli karıştırıcı altında 10 mM konsantrasyonda mutlak etanol içinde çözündürüldü, Cam substratın slayt üzerine 25ML damlacık çözeltisi kaplandı, kaplanmış substrat sıcak bir plaka üzerinde $55°C$'de kurutuldu, bu kaplanmış adım tekrarlandı birkaç kez 25 kez ve daha sonra çok katmanlı ZnO tohumunu vermek için havada 30 dakika boyunca $350°C$ 'de tavlandı.
Daha sonra, ZnO tohumları, hidrotermal bir otoklavda 25 mM hidratlanmış çinko nitrat ve heksaminin 100 ml eşmolar sulu (Deiyonize su) çözeltisinde büyütülür, ZnO tohum tabakası kaplı kayar cam substrat, otomatik bölmede baş aşağı sulu çözeltiye daldırılır ve konur. fırına 10 saat boyunca $150°C$ 'de koyun, son olarak büyütmeden sonra substrat deiyonize su ile yıkanır ve havada kurutulur. ayrıca, nihayet büyüme nanorodları için 30 dakika boyunca 300°C'de halka açıldı. aynı durum altında farklı konsantrasyonlarda ZnO ile doping ve kodoping (Y ve Mg) için tekrarlanan hidrotermal otoklav.

## 1.4 Wien2k Hesaplamali Program

Atomik yapıların optik ve elektronik özelliklerini teorik olarak hesaplamak oldukça zordur. Bu sorunun üstesinden gelmek için farklı özelliklere sahip bilgisayar destekli hesaplama programları kullanılır. Bu programlar WİEN2k, ABINIT, SİESTA, Quantum ESPRESSO, VASP vb. simülasyon programlarıdır.

Bu tezde saf ve Mg katkılı ZnO kristalinin incelenmesi için WİEN2k programı kullanılmıştır. WIEN2k (Blaha,et,al.,2020) programı DFT'ye dayanır ve Kohn-Sham denklemlerini çözmek için artırılmış düzlem dalgası artı yerel yörüngeler (APW + lo)

kullanır. Elektronik bant yapısı, optimize edilmiş atomik yapı, vb. Gibi birçok özellik hesaplanabilir (Blaha et al., 2020).

APW'nin genişletilmiş bir versiyonu olan APW (Augmented Plane Wave) yöntemini ve LAPW (doğrusal olarak artırılmış düzlem dalgası) yöntemini kullanır. Ayrıca, GGA ve LDA yaklaşımlarının türevleri olan PBE-GGA, PBEsol-GGA, WC-GGA ve LSDA yardımıyla değişim ve korelasyon enerjisini sürece dahil eder.

## 2.SONUÇLAR VE TARTIŞMA

### 2.1 Optik özellikler

Hidrotermal teknikle hazırlanmış (x =% 0,% 5 ve% 10) filmlerle saf ve $Zn_{90}\ Y_x\ Mg_{10-x}$ formülü kullanılarak elde edilen O'nun optik özellikleri. Hazırlanan tüm numuneler, absorbans ve geçirgenlik verilerini elde etmek için 300 nm ila 900 nm aralığında UV-VIS spektroskopisi kullanılarak ölçülür. Optik enerji açığı, Tauc denklemi kullanılarak hesaplandı.

### 2.2 Optik enerji bant aralığı

Enerji bant aralığı film yapısına, kristal kafesteki atomların düzenine, dağılımına ve kristal dizilimine bağlıdır. Daha önce yapılan çalışmalar da ZnO'nun direk bant geçişine sahip olduğunu görülmüştür (Narayanan, 2016). Bu bilgiler kullanılarak, optik enerji aralığı,$E_g$ , aşağıdaki formülle tüm numuneler için Taug denklemi kullanılarak hesaplandı.

$$(Ahv)^{\frac{1}{n}} = A\left(hv - E_g\right) \tag{47}$$

burada h Planck sabiti, υ fotonun frekansı, α soğurma katsayısı, $E_g$ bant aralığı ve A sabittir. Bizim durumumuzda n, çinko oksit ince filmler de izin verilen doğrudan geçişler için ½'ye eşittir. Düz çizginin $(\alpha\ hv)^2 = 0$ değeri, malzemenin doğrudan bant aralığının değerini verir, $(\alpha hv)^2$ 'nin hv'ye bağımlılığı şekil (2.1) 'te gösterilmiştir. Bu şekilden elde edilen $E_g$ değerleri, 3.262, 3.18, 3.31, 3.07, 3.157 eV, alt tabaka katmanı (seed layer) ZnO, $Zn_{90}\ Mg_{10}\ O$, $Zn_{90}Y_{10}\ O$ ve $Zn_{90}\ Mg_5\ Y_5\ O$, olarak ölçülmüştür.

Kritik değere kadar kristal boyutunda bir azalma (kritik değer, kuantum etkisini başlatan belirli bir değerdir), bant aralığının azalmasına (kırmızı bölgeye kayma) ve kritik değerin altındaki değerler için (mavi bölgeye kayma).
Genel olarak sonuç, dopingin enerji bandı boşluğunu nasıl etkilediğini gösterdi.

Şekil (2.1a) tavlama işleminden sonra ZnO alt tabaka katmanı için enerji bant aralığını 3.262eV olarak göstermektedir. Şekil (2.1b) 'den, saf ZnO için enerji bant aralığı autoclave tekniklerinden sonra 3.18 eV'dir. Auto clave sonra numunenin bant aralığı değeri, alt tabaka bant aralığına kıyasla azalır. Tavlama sonrası davranış, filmin sıcaklığı, partikül boyutu ve modifikasyon yapısı ile açıklanabilir.

ZnO: Mg durumunda, bant aralığı 3.31 eV olarak hesaplanır. Bu bant aralığı, önceki deneysel çalışmayla iyi bir uyum sağlar (Inbaraj et al.,2018). Gözlenen değer daha düşük dalga boyuna kaydırıldı, kaymanın ötesindeki sebep, $Mg^{+2}$ 'nın $Zn^{+2}$' ya kıyasla daha küçük iyonik yarıçapından kaynaklanıyor olabilir (Islam, et al., 2020). Bant aralığındaki bu tür bir artış, Burnstein – Moss etkisine bağlanabilir (Kara et al., 2020).

Y katkılı ZnO durumu, $E_g$is 3.07 eV (kırmızıya kaymış) olarak hesaplandı. Bu değer, katkılanmamış örneğe göre daha düşük olarak ölçülmüştür. Bu sonuç, büyüme sırasında meydana gelen kristal boyutunun küçülmesi ve tane sınırı konfigürasyonunun modifikasyonu olarak açıklanabilir (Kaur, 2004).

Şekil (2.1e) 'den, enerji bandı aralığı $Zn_{90}\ Mg_5\ Y_5\ O$ için 3.157eV gözlenmiştir. Bu değer Y katkılı ZnO'dan daha yüksek, ancak saf ve Mg katkılı ZnO durumundan düşüktür. Bu enerji bandı boşluğu değeri, Y'nin yasaklanmış enerji bandı aralığı üzerindeki etkilerinin Mg durumuna göre baskın olduğunu ifade etmektedir. Dahası, bu sonuç, takviye edici elementlerin itriyum ve magnezyumun yasaklanmış enerji bant aralığı üzerindeki etkisinden kaynaklanıyor olabilir.

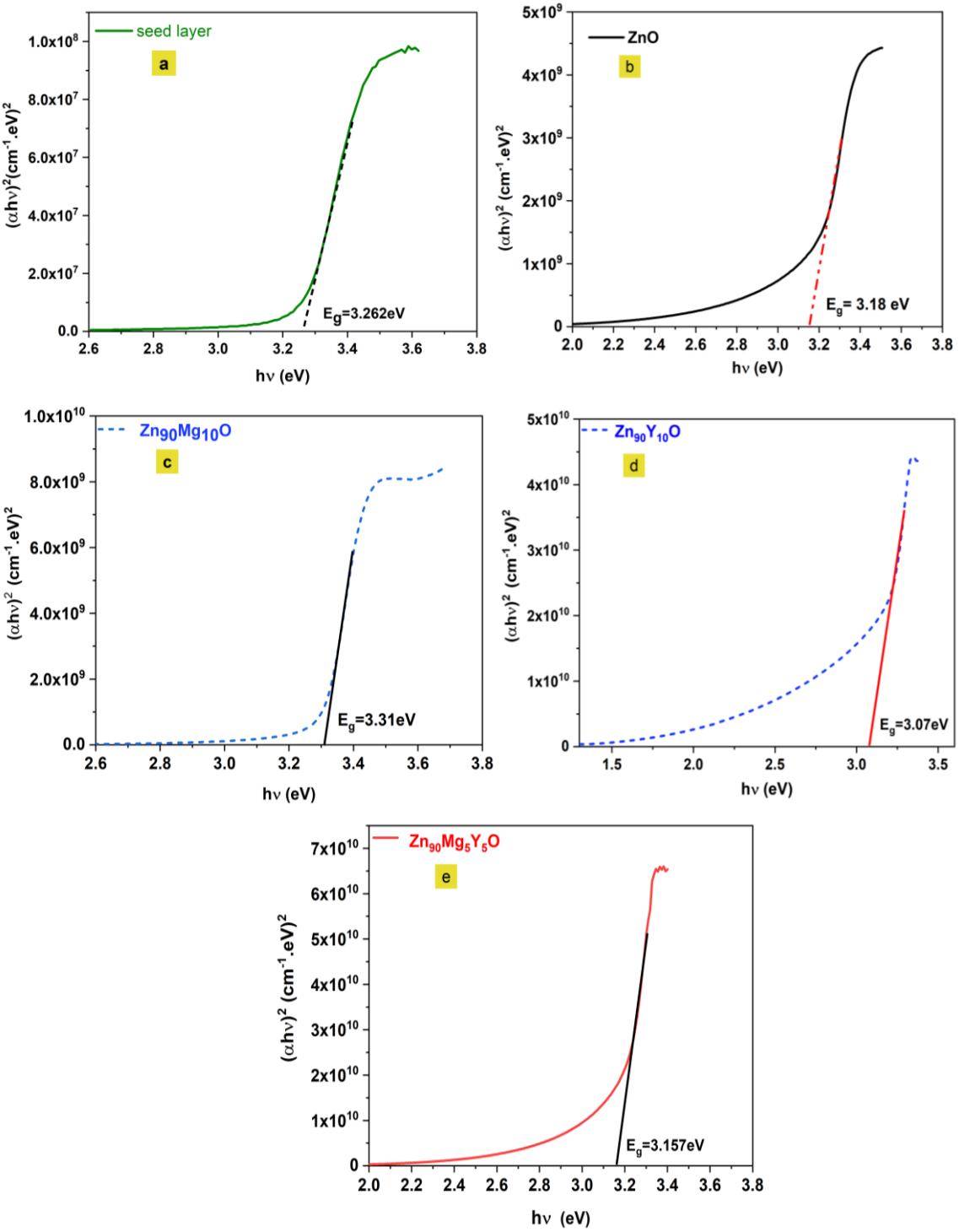


Şekil 5.3. İçin enerji bant aralığını gösterir (a) seed layer, (b)ZnO, (c) $Zn_{90}Mg_{10}O$, (d) $Zn_{90}Y_{10}O$.(e) $Zn_{90}Mg_5Y_5O$

## 2.3 Teorik Çalışma

### 2.3.1 Saf ve katkılı ZnO'nun elektronik özellikleri

ZnO'da en çok araştırılan özelliklerden biri elektronik özelliklerdir. Hesaplanan enerji bandı yapısı ve yoğunluk durumları, ZnO'nun elektron özelliklerini ortaya çıkarır. Şekil (2.2), PBEsol potansiyelini kullanarak çinko karışımının elektron bandı yapısını göstermektedir. ZnO'nun, valans bandının üstü ve iletim bandının alt kısmı aynı yüksek simetri noktası olan gama noktasında yer aldığından, doğrudan bir bant aralığı geçişine sahip olduğu görülebilir.

Şekil (2.2), enerji aralığının -4 ile 8 eV arasındaki enerji bandı yapısını göstermektedir. Yasak boşluk enerjisinin, saf durum için 0.67eV olduğu görülmektedir. Sonuçlar, LDA ve GGA'da kullanılan ZnO'nun enerji bant aralığı 0,64 ile 0,813 arasında çalışılan diğer araştırmacılarla uyumludur (Yaakob ve diğerleri, 2014). Ve sonucumuz, bağlanma enerjisini küçümseyen GGA'nın doğası nedeniyle deneysel değerden daha düşük.
d urumunda anyon p valans hibridizasyonuna neden olur. Güçlü bir p-d bağlantısı sonunda daha küçük bir bant aralığı sağladı. Bunlar, şekil (2.3) 'da PBEsol + hf kullanılarak çözülebilir.

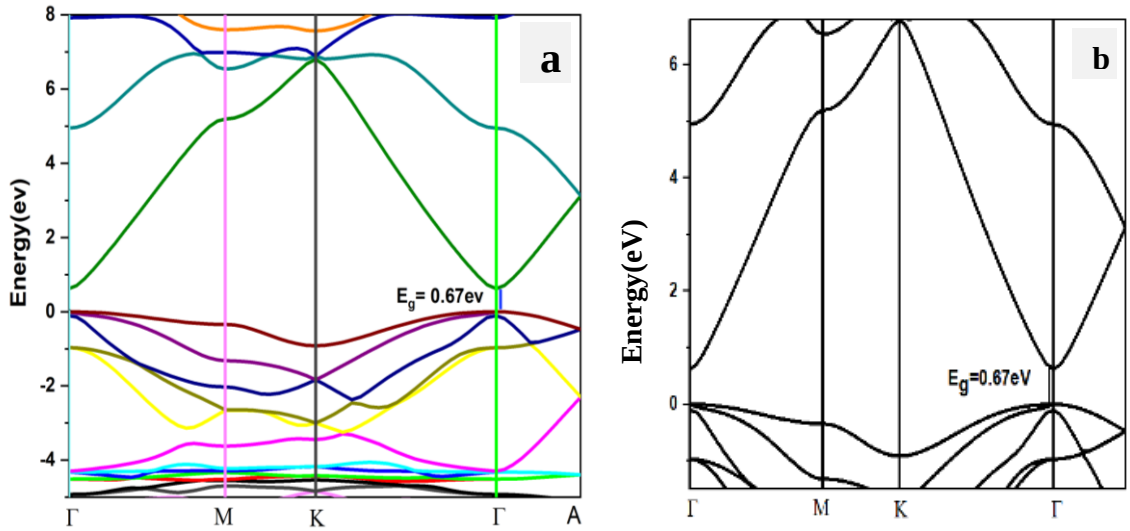


Şekil 2.2 . PBEsol ile ZnO için bant yapısını gösterir.

Şekil (2.3), PBEsol potansiyeli kullanılarak yasaklanmış bant aralığı üzerindeki katkılamanın etkisini göstermektedir. Mg katkılı ZnO, yasak bant aralığının daha yüksek enerji değeri olan 0.89eV'ye kaymasına neden olur. Bu, maviye kaymanın, $Zn^{+2}$ (0.83 Å) a kıyasla $Mg^{+2}$ (0.78 Å) ın daha küçük iyonik yarıçapından kaynaklanabileceğini gösterir (Islam et al. 2020). Bu nedenle yasak bant aralığı artırılır.

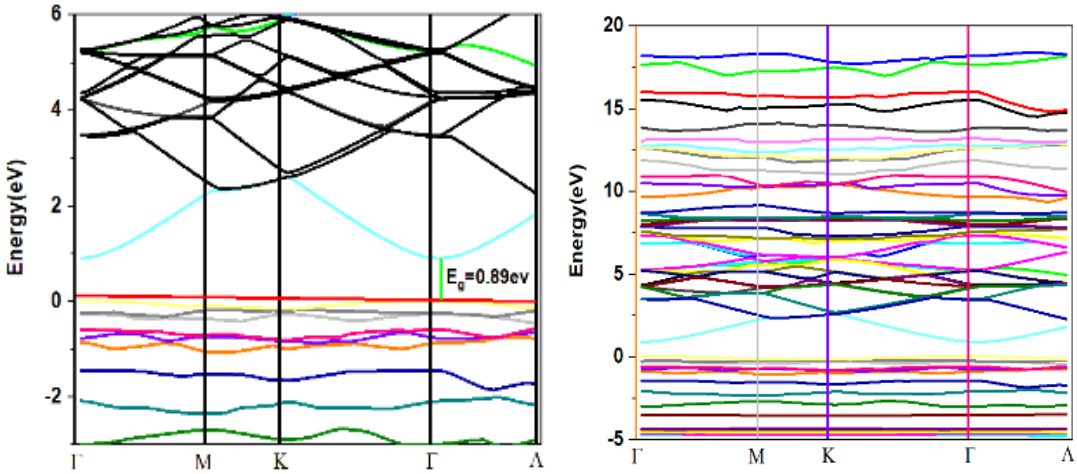


Şekil 2.3. Mg katkılı ZnO için yasak bant yapısını gösterir.

Şekil (2.4), PBE-sol'a bir hibrit fonksiyon eklenmesinin yasak enerji bandının 2.47eV'ye yükseldiğini gösterdi. bu sonuç daha doğru ve deneysel çalışmaya yakındır.

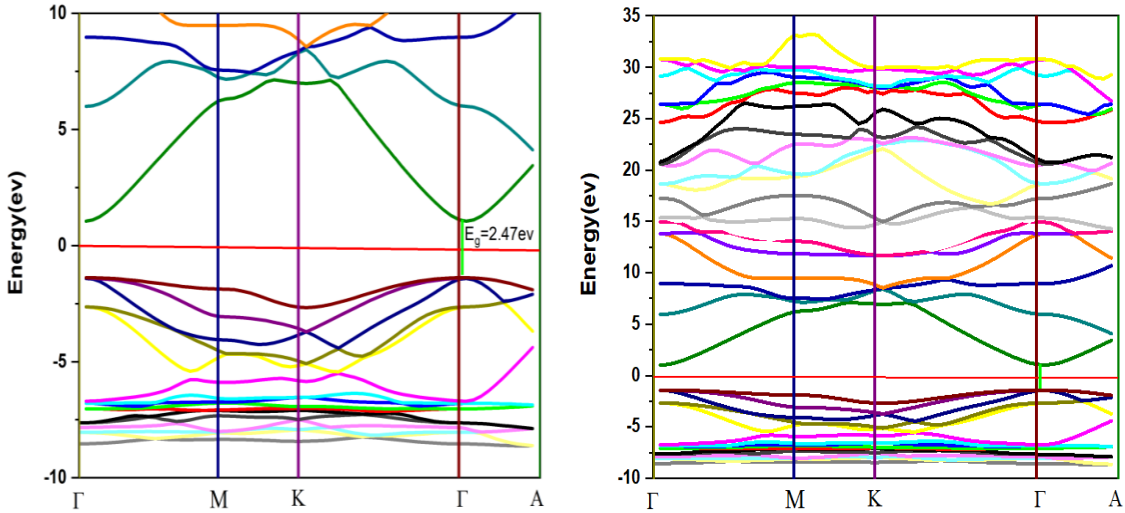


Şekil 2.4 PBEsol + hf için bant yapısını gösterir.

**SONUÇ**

Saf ve Mg, Y ve Mg-Y ortak katkılı ZnO bileşikleri deneysel ve teorik yöntemlerle yasaklanmış enerji bandı boşluğuna katkı maddesinin etkisini belirlemek için incelenmiştir. Deney bölümünde, numunelerin hazırlanması için hidrotermal yönteme ihtiyaç duyulmuştur. Otoklavın verileri etkilemediği sonuçları bulmak. Mg katkılı ZnO numunesi saf duruma göre absorbans kaymış mavi bölgeye sahipken, Y ve Mg-Y birlikte katkılı ZnO'nun absorbansı mor bölgeye kaymıştır.

Teorik kısımlarda, gelen kirişin geçiş hızının doping elemanının cinsine göre değiştiğini göstermektedir. Gelen dalganın% 10'unda iletilen Mg katkılı Zn, daha düşük seviyeyi etkiledi, ancak Y katkılı ve Mg-Y ortak katkılı ZnO, gelen dalga ışığının yarısını örneğe iletti. UV-vis ölçümlerinden görüldüğü gibi, katkılı ve saf ZnO'nun yasak bant aralığı, doping durumuna göre değişmiştir. Mg dopped gibi bant aralığı artırılır ve tersine dopped, Y ve co-doped ile yasak bant aralığı azalır. Absorbans, geçirgenliğin tersidir, doping durumuna bağlı olarak değişir

# CURRICULUM VITAE

**Mahmood H. Majeed**

**Date and place of birth:**

**E-mail:** mahmoodhameed1990@gmail.com

**Phone number:**(+90)5352776381, (+964) 7501637793

**Address:** Physics department, College of Education, University of Garmian, Kalar, As Sulaymaniyah, Iraq

---

- **Educational status:**

  B.Sc. of physics, University of Sulaimanyah, average grade: 71.545 of 100, stood as 2nd student of 22 graduated from the first trial, 2012-2013.

  02/2019 Continues study M. Sc with thesis – Solid state physics in Van Yuzuncu Yil University – Institute of natural and applied Science – Physics Depatment.

- **Academic work status:**

  Employed as Lab. Assistant in Phys. Dept. of the University of Garmian from 2013 until now.

- **Research and technical skills:**

  Thin-film formation by chemical vapour deposition (CVD), spray pyrolysis (SP), hydrothermal and spin coating method.

- **Computer skills:**

  Matlab, LaTex, SPSS, Origin, Mathcad, Office.

- **Language skills:**

  Kurdish (mother tongue)
  Arabic (intermediate)
  English (intermediate)
  Turkish (beginner )